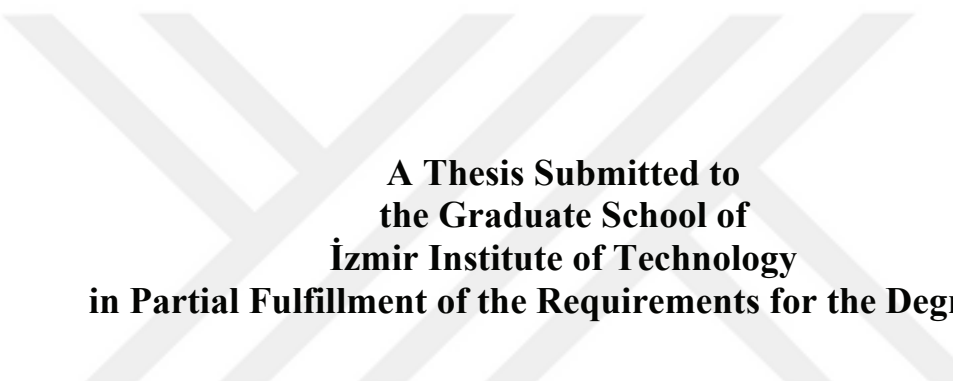# COMPARISON OF POWDER SYNTHESIS METHODS FOR THE PRODUCTION OF POTASSIUM SODIUM NIOBATE (KNN)

**A Thesis Submitted to
the Graduate School of
İzmir Institute of Technology
in Partial Fulfillment of the Requirements for the Degree of**

MASTER OF SCIENCE

in Materials Science and Engineering

**by
Cerem PİŞKİN**

**July 2021
İZMİR**

ACKNOWLEDGMENTS

ABSTRACT

COMPARISION OF POWDER SYNTHESIS METHODS FOR THE PRODUCTION OF POTASSIUM SODIUM NIOBATE (KNN)

Alkali niobate-based, i.e., potassium sodium niobate, $K_xNa_{x-1}NbO_3$ at x=0.5 (the composition at the morphotropic phase boundary (MPB)), based materials have been reported as promising lead-free piezoelectrics to be substituted with the most extensive lead-based, i.e., lead zirconate titanate (PZT) ones. In this thesis, KNN particles were obtained using three discrete powder synthesis routes: conventional solid-state reaction, hydrothermal synthesis, and sol-gel processing. The as-synthesized powders were characterized via several techniques to provide a comparative study and underline the difficulties upon KNN synthesis. In the conventional method, the phase pure $K_{0.5}Na_{0.5}NbO_3$ powders were obtained at 850°C with 382 ∓ 68 nm particle size. Unfortunately, the process cannot be considered sustainable due to the high risk of non-perovskite impurity phase formations. Also, the results demonstrated that single phase KNN powder having the MPB composition could not be accomplished via a one-step hydrothermal reaction process because of the inevitable formation of the second $NaNbO_3$ phase. Instead, post-heat treatment of biphasic (K-rich (x>0.5) KNN and $NaNbO_3$) samples lead to induction of sodium incorporation into the crystal lattice. Eventually, phase-pure KNN particles with high proximity (x=0.58) to MPB were achieved. The KNN powder with the smallest particle size (145 nm) was obtained using the sol-gel method at 500°C. However, the samples showed carbonate impurities resulting from the reaction of unreacted alkali cations (K^+ and/or Na^+) with the ambient CO_2. Hence, the KNN samples needed to be stored under an inert atmosphere to ensure purity.

ÖZET

POTASYUM SODYUM NİYOBAT (KNN) ÜRETİMİNDE TOZ SENTEZ YÖNTEMLERİNİN KARŞILAŞTIRILMASI

Alkali niyobat bazlı, potasyum sodyum niyobat, x=0.5(morfotropik faz sınırına (MPB) denk gelen kompozisyon) için $K_xNa_{x-1}NbO_3$, malzemelerin en yaygın olarak kullanılan, kurşun bazlı kurşun zirkonat titanatların (PZT) ikamesi olarak kullanılmak üzere umut verici olduğu raporlanmıştır. Bu tezde, KNN partikülleri üç ayrı toz sentezi yolu kullanılarak elde edildi: geleneksel katı hal reaksiyonu, hidrotermal sentez ve sol-jel yöntemi. Sentezlenen tozlar, karşılaştırmalı bir çalışma sağlamak ve KNN sentezindeki zorlukların altını çizmek için çeşitli yöntemlerle karakterize edildi. Geleneksel yöntemde, perovskit olmayan safsızlık oluşumlarının yüksek riski nedeniyle bu yöntem sürdürebilir bulunmamıştır. Ayrıca sonuçlar, MPB bileşimine sahip tek fazlı KNN tozunun, ikinci NaNbO3 fazının kaçınılmaz oluşumu nedeniyle, tek aşamalı hidrotermal reaksiyon işlemi ile gerçekleştirilemeyeceğini göstermiştir. Bunun yerine, bifazik (K açısından zengin (x>0.5) KNN ve $NaNbO_3$ fazlarından oluşan) numunenin ısıl işlemi sonrası kristal kafese sodyum katılımı tetiklenmiş ve nihayetinde MPB'ye yüksek yakınlıkta (x=0.58) saf KNN parçacıkları elde edilmiştir. En küçük partikül boyutuna (145 nm) sahip KNN tozu, 500°C'de sol-jel yöntemi kullanılarak elde edilmiştir. Ancak numuneler, reakte olmamış alkali katyonların (K^+ ve/veya Na^+) ortamdaki CO_2 ile reaksiyonundan kaynaklanan karbonat safsızlıkları göstermiştir. Bu nedenle, saflığı sağlamak için KNN numunelerinin inert atmosferde saklanması gerekmektedir.

TABLE OF CONTENTS

LIST OF FIGURES

LIST OF TABLES

CHAPTER 1

INTRODUCTION AND MOTIVATION

Piezoelectrics are materials having the ability to generate an electric field when they are exposed to mechanical stress, and which is called the direct piezoelectric effect. It operates reversibly as well, meaning that it is also possible to produce mechanical stress as a result of applied electrical field[1]. This group of functional materials has various applications in pressure sensors, surface acoustic wave (SAW) devices, ultrasonic transducers and motors, piezoelectric transformers, and actuators and so on[2, 3].

Piezoelectricity was first discovered by the Curie brothers in quartz crystal. Then, piezoelectricity of $BaTiO_3$ (BT) and lead zirconia titanate (PZT) were discovered, respectively. Detailed historical evaluation is demonstrated in Figure 1.1[3]. Among piezoelectric materials, lead zirconate titanate (PZT) has been dominating the market due to its electromechanical properties[3, 4]. However, PZT ceramics have a lead content of more than 60 weight percent[5]. Taking into consideration its high toxicity and relatively high vapor pressure, heat treatments at elevated temperatures, e.g., calcination, sintering, etc., increase lead release to the atmosphere[1]. In addition to its toxicity, recycling and storage of lead oxide also pose challenging problems[4, 6]. Lately, governmental regulations aiming at limiting the use of hazardous substances were introduced. For example, the European Union received two directives, Waste Electrical and Electronic Equipment (WEEE) and Restriction of the use of certain Hazardous Substances (RoHS)[7, 8]. Therefore, substituting lead-based piezoelectrics such as PZT with safer ones became urgent. As a result, a new materials group called lead-free piezoelectric materials purposed to be replaced with lead-contained ones[1].
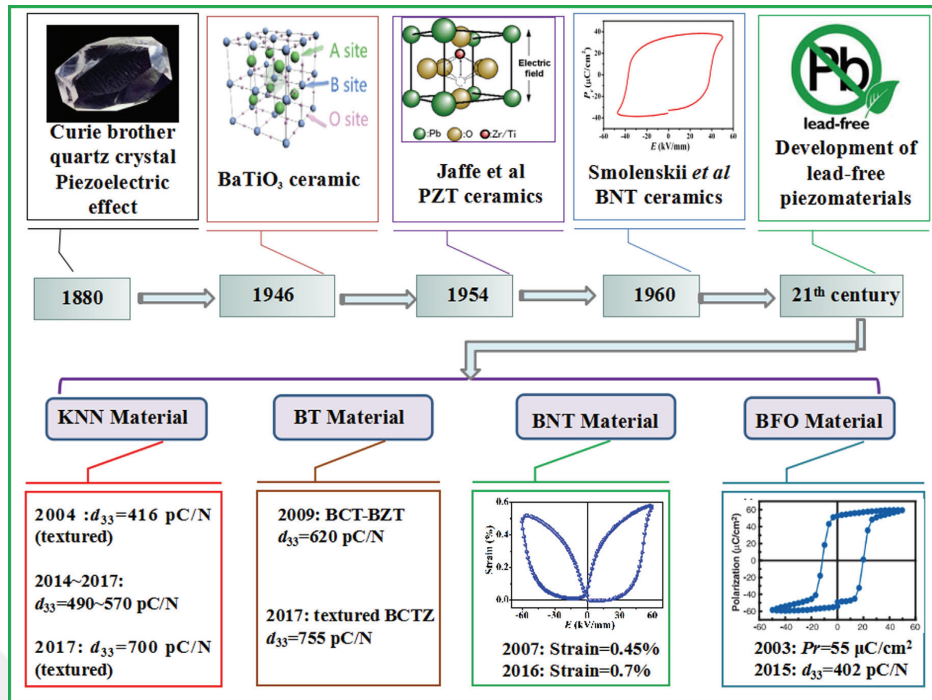
Figure 1.1. Historical development of piezoelectrics
(Source: Zheng, 2018) [3].

The most studied lead-free piezoceramics may be classified as perovskite, bismuth layered, and tungsten bronze structures[3]. Among those, perovskite structured piezoelectrics have received significant attention due to their enhanced piezoelectricity. A schematic representation of cubic perovskite structure is given in Figure 1.2, in which the green, red and blue spheres represent A cations, B cations, and oxygens, respectively. The symmetrically positioned atoms yield smooth deformation and polarization (see the polarized structure Figure 1.2(b)), which can be considered essential for material to expose piezoelectricity[1]. Perovskite materials have the general chemical formula of ABO_3, where A and B are two different cations having a different atomic size. In a general manner, the atomic radius of A cations are larger than that of B cations. In the perovskite structure, the atoms are arranged to form a corner-sharing of the smaller cations octahedra (BO_6) network (see the octahedra in Figure 1.2(b))[1, 9, 10].
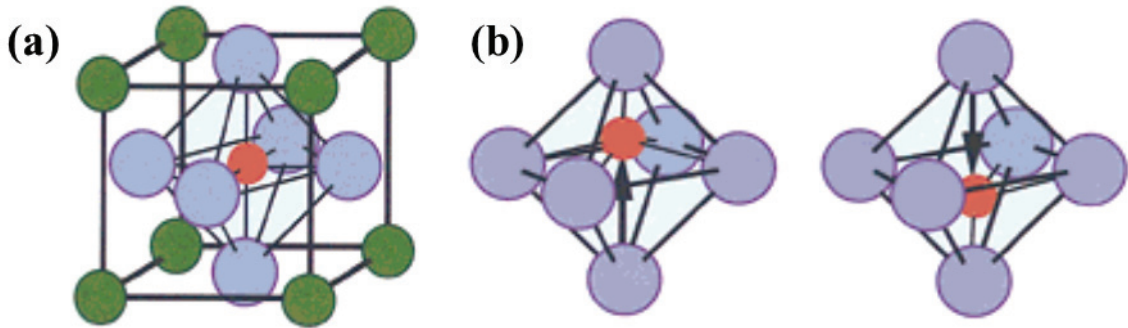
Figure 1.2. The unit cell of a cubic perovskite crystal(A, B, and oxygen atoms are represented with green, red, and blue spheres) (Source: Haertling, 1999) [10].

The basic parameters to be considered during the evaluation of piezoelectric performance can be sorted as a piezoelectric coefficient (d_{33} in pC/N) and Curie temperature (T_C in °C)[2]. The higher those parameters, the better the piezoelectricity gets, e.g., higher Curie temperature is desirable for the stability of the piezoelectric effect at elevated temperatures[1]. The influence of the stoichiometric composition on electrical properties was first investigated by Jaffe et al.[11]. After then, it was realized that a structural change occurs in solid solutions for specific compositions regardless of the temperature. This change originates from an unstable phase compared to another one and results in the coexistence of two crystal phases[9, 12]. Therefore, the polarized dipoles are able to orient more comfortably, yielding enlarged electrical properties, in particular, piezoelectricity[2, 12].

Lead – free perovskite structured piezoelectrics include $K_{0.5}Na_{0.5}NbO_3$ (KNN), $BaTiO_3$ (BT), $Bi_{0.5}Na_{0.5}TiO_3$ (BNT), $BiFeO_3$ (BFO)[1, 3]. Among those, alkali niobate-based, e.g. $K_{0.5}Na_{0.5}NbO_3$ (KNN, 0<x<1), has been investigated the most owing to its promising piezoelectric coefficient ($d_{33} = 80$ pC/N)[13] and high Curie temperature ($T_C = 415$°C)[12].

Potassium Sodium Niobate ($K_xNa_{1-x}NbO_3$) is a lead-free piezoelectric material being a complete solid solution of antiferroelectric $NaNbO_3$ and ferroelectric $KNbO_3$[14]. The specific composition studied the most is with x ~ 0.5 ($K_{0.5}Na_{0.5}NbO_3$), where the piezoelectric effect reaches its maximum owing to being close to the morphotropic phase boundary (MPB)[14, 15]. Despite being a good substitution for lead-based piezoelectric

materials, KNN-based ceramics had a piezoelectric coefficient which was still insufficient to compete with commercial PZT (d_{33} = 200 – 590 pC/N)[3, 4]. However, Saito et al.[16] changed the approach by managing produce textured KNN-based piezoceramics with piezoelectricity coefficient reaching up to 416 pC/N, which is superior to soft and few hard PZT ceramics, e.g., acceptor (Fe^{3+}) doped PZT (225-285 pC/N)[17]. Piezoelectric coefficient and Curie temperature values of various KNN-based solid solution systems are tabulated in Table 1.1. Further development in the piezoelectricity constant has been reported[18], despite being a quite complex composition.

Table 1.1. Piezoelectric coefficients of KNN-based ceramics

Composition	d_{33} (pC/N)	T_C (°C)	Reference
KNN	80	420	13
KNN	160	420	19
KNN + 0.5 mol% ($K_4CuNb_8O_{23}$)	180	402	20
KNN + Li,Ta,Sb (Textured)	416	253	16
KNN + 6 mol% $LiNbO_3$	235	475	21
KNN + 2-3 mol% BNT	195	375	22
KNNS-CZ-BKH ($K_{0.5}Na_{0.5}$) ($Nb_{0.965}Sb_{0.035}$)-$CaZrO_3$-($Bi_{0.5}K_{0.5}$) HfO_3 + 3 mol% $NaNbO_3$ (Textured)	700	242	18

There are also disadvantages considering the high sensitivity of the electrical properties of $K_xNa_{1-x}NbO_3$ – based piezoceramics, in particular on the stoichiometric composition. Hence, preserving the stoichiometry, i.e., keeping x ~ 0.5, becomes a crucial issue during both powder synthesis and monolith production[23]. Nevertheless, it is challenging to obtain KNN powder at the exact MPB composition. Besides, the structural characterization of such composition poses further challenges when XRD analysis was used since the only difference between the XRD patterns of three discrete niobate phases, i.e., $NaNbO_3$, $K_{0.5}Na_{0.5}NbO_3$, and $NaNbO_3$, is a peak shift of 0.2°(2θ).

Despite many studies focused on the synthesis of KNN, there have been no reports in which a systematic and repeatable procedure was provided. Accordingly, the aim of this thesis study was based on to provide a comprehensive study comparing the outcomes of the three distinct powder synthesis methods such as conventional solid state synthesis, hydrothermal reaction, and sol-gel processing for KNN production. In addition to that, numerous Rietveld refinements have been performed to highlight those considerations.

CHAPTER 2

LITERATURE SURVEY

2.1 Powder synthesis methods

The most commonly applied powder synthesis method for KNN is the conventional solid-state reaction. Apart from that, alternative methods such as molten salt synthesis[24-26], sol-gel processing[27-29], co-precipitation[30], spray pyrolysis[31], hydrothermal[32-36], and solvothermal reaction[37, 38] have also been purposed.

2.1.1 Solid-State Reaction

The solid-state reaction is one of the oldest and most common techniques that is used for the preparation of ceramic powders due to its capability of production on an industrial scale. It is based on a solid-solid reaction between oxide and carbonate precursors.

According to the technique, the raw materials may need to undergo pre-treatment processes such as drying for the avoidance of their hygroscopic nature or individual ball milling to obtain a reduced, homogeneous particle size distribution[39]. Then, the reactants are mixed and grounded by a planetary ball mill, shown in Figure 2.1(a), using an appropriate medium, e.g., ethanol, acetone, isopropanol, etc., to obtain a homogeneously dispersed powder. The cross-section of the milling jar is given in Figure 2.1(b), where A, B, C, and D represent the slurry consisting of the medium and precursors, ball collisions, agglomerated precursors on the surface of the balls, and falling balls through the slurry, respectively[40].
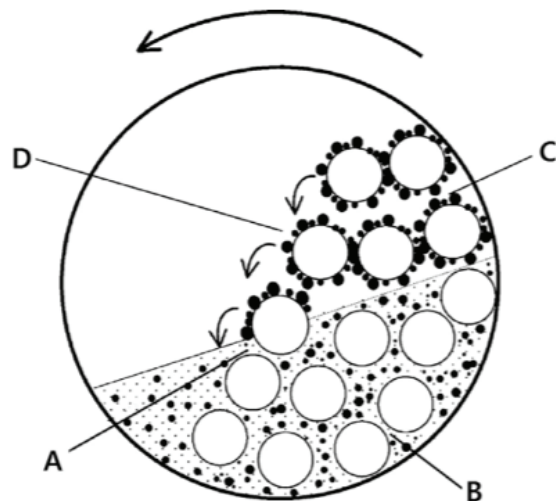
Figure 2.1. (a) Planetary ball mill; (b) cross-section of the milling jar
(Source: Shin, 2013)[40].

This process is followed by the calcination stage, where the products form at the interfaces of the raw materials, as shown in Figure 2.2 for perovskite structured materials. Hence, the reaction rate is highly dependent on the diffusion rate of reactants through the mentioned interfaces[41]. The temperature for calcination can be as high as 1200°C, e.g., for magnesium aluminate ($MgAl_2O_4$)[39], depending on the material. The value has been reported as within the range of 600 - 900°C[42, 43].
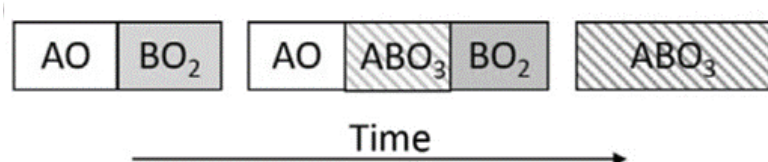
Figure 2.2. Solid-state reaction
(Source: Malič, 2018)[41].

The benefits of this method include simplicity of the process and ease to scale up for large amounts of synthesis[44]. Also, plenty of experimental data can be found in the

literature since it is one of the most widely used methods[45]. However, the solid phase reaction needs to be carried out at high temperatures. Hence, the process becomes highly energy-consuming[46]. Unfortunately, treatment at elevated temperatures arises another drawback that is the inevitable agglomeration of particles. Such a case leads to large particles, e.g., generally around 1 μm[39]. Although particle size reduction can be accomplished via further milling, there is a significant risk of contamination during the process, which results in low purity products[44, 47].

During the conventional synthesis of KNN, there is the need for alkali carbonate precursors, which are strongly in a tendency to absorb moisture, ensuring the purity of raw materials requires great care[23, 48]. Such care may involve processing under a controlled atmosphere, e.g., under N_2, or pre-heat treatment of the raw materials to eliminate the absorbed moisture[5]. Additionally, it is difficult to control the stoichiometry under processes involving high temperatures (>800°C), e.g., calcination for conventional solid-state synthesis. This is because of the relatively high volatility of alkali oxides (Na_2O and K_2O)[23]. Also, thermodynamic calculations have shown that the vapor pressure of K_2O is higher than Na_2O as it already has a lower melting point (740°C) compared to Na_2O (1134°C)[31]. Hence, uneven volatilization takes place and may cause precipitation of a secondary Na-rich phase in the form of unusual grains[49], deviations from the stoichiometry, and formation of non-perovskite structures[50]. Reduction of calcination temperature could be the key to this problem and it was achieved by reducing the particle size through a high-energy ball milling process[6]. However, contamination by the balls or the vessel problem came up as it is known that conventional powder synthesis facilitates insufficient purity, which is one of its main drawbacks[39].

2.1.2 Mechanochemical Activation

The mechanochemical activation resembles the solid-state reaction method. However, the reaction is accomplished by the application of mechanical energy instead of thermal energy[51]. In other words, the reactants are subjected to a high-energy ball milling process at high rotations. Such a process causes plastic deformation, the disordering of grain boundaries, crystallographic defects, and broken bonds.

Consequently, an excess amount of energy arises, leading to the formation of a new, chemically active form of energy. Hence, the application of external thermal energy becomes unnecessary[52]. Figure 2.3 demonstrates the progress during high-energy ball milling, where the large particles are enclosed between the balls in Figure 2.3(a), crack propagation and fracture follow that stage in Figure 2.3(b), and finally, particle size refinement is shown in Figure 2.3(c)[53].
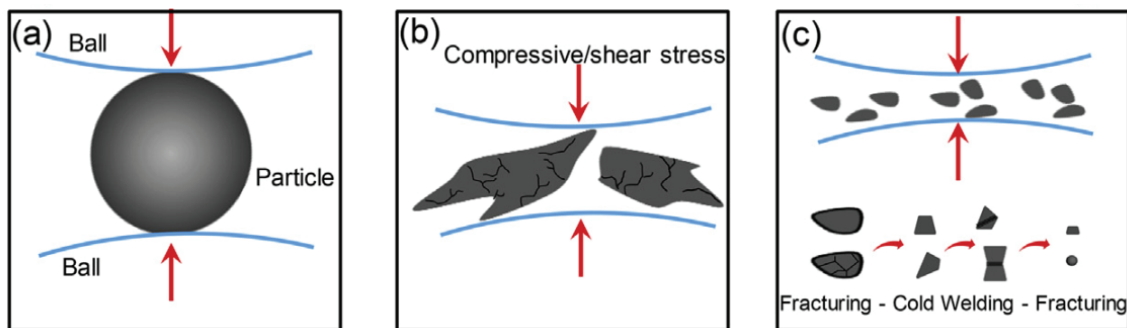
Figure 2.3. The high-energy ball milling process
(Source: Ambika, 2016)[53].

The main advantage of mechanochemical activation is that it is readily performed in industry since it is capable of producing a large amount of product[54]. Also, it is a simple, single-step process, just like the solid-state reaction method. Nevertheless, although there is no heat application system, it is still an energy-consuming process because of extensive mechanical energy requirements. Similar to the solid-state route, there is also a high contamination threat that yields low purity products. Besides, obtaining a new product with a small particle size may be time-consuming due to the necessity of large milling time[46].

2.1.3 Molten Salt Method

The molten salt method relies on generating an ion pool by melting salt, and using it as a solvent and/or as a reactant[44]. In a general manner, the eutectic mixtures of sulfate or chloride salts are preferred to lower the temperature. For instance, NaCl and KCl have melting points of 801°C and 770°C, respectively. And their eutectic mixture's melting point is 650°C. After heat treatment, the mixture needs to be washed several times to eliminate excess salt. The product is obtained after drying as visualized in Figure 2.4[55].
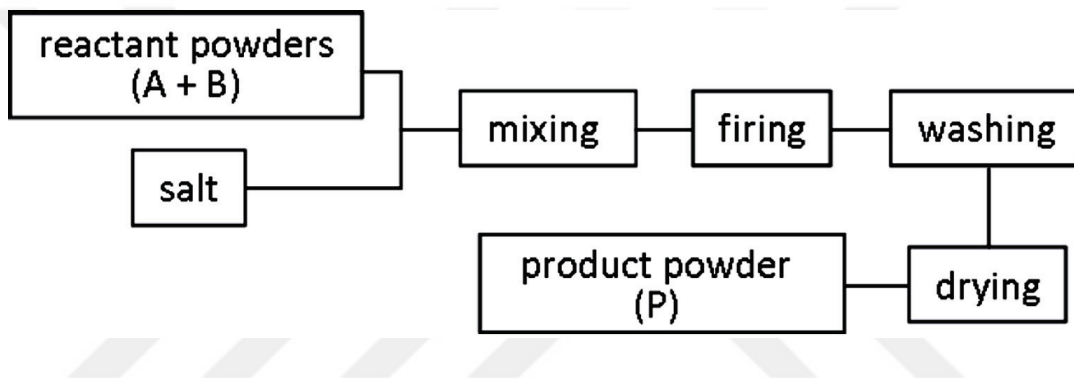
Figure 2.4. Molten salt method
(Source: Sikalidis, 2011)[55].

During the reaction, the product particles form via heterogeneous nucleation at the surface of the reactants, which functions as nucleation sites. The amount of salt is generally adjusted as 80-120 wt% of reactant mixture because it is enough to coat those nucleation sites. The criteria for salt selection include being available, inexpensive, easily washed away, and having a low melting point and vapor pressure. The molten salt has several functions, such as increasing the reaction rate, lowering the reaction temperature, controlling the particle size, etc[55].

Molten salt is a preferred method due to its available precursor and simplicity. Yet, the amount of salt needs great cation. It is substantial to introduce all the required amounts of salt to coat nucleation sites, i.e., reactant surfaces. If the necessary amount of salt does not present in the system, the expected liquid phase cannot be achieved. On the

other hand, using too much salt has two unfortunate consequences. One is that the excessive salt causes the phase separation of the reactants due to the sedimentation. Such a case significantly decreases the reaction rate. The latter is that the excess salt solidifies and adheres to the walls of the reaction vessel[55].

2.1.4 Sol-gel Processing

The term sol means colloidal dispersion of nano-sized particles in a liquid[56]. Such a mixture undergoes a gelation process where the nano-sized particles are aggregated under appropriate conditions by a solvent removal process or a chemical reaction[39]. The gelation process of the particles is visualized in Figure 2.5, where the first image and last images represent the sol and complete gelation phases, recpectively[57]. The gel stage can be expressed as three-dimensional inorganic networks where the polymers act as the linkage components[56, 58].
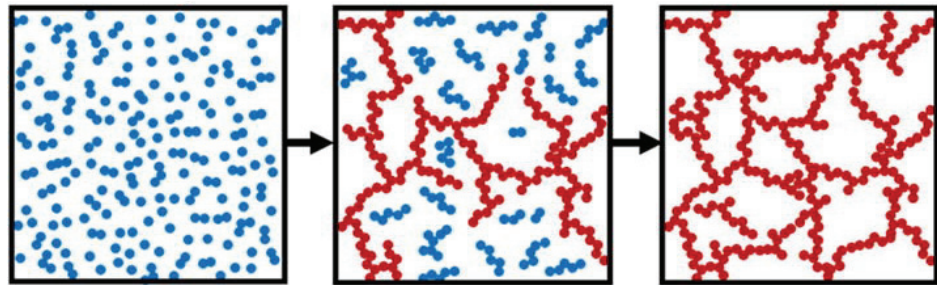
Figure 2.5. Gelation process

(Source: Liu, 2019)[57].

Figure 2.6 demonstrates a more detailed image of sol-gel processing[59]. First, the precursors are hydrolyzed, i.e., water disengages the bonds, and pushes the mixture into a sol. Subsequently, the polycondensation reaction takes place. In addition to the elimination of the excess water, bridging oxygen atoms form the three-dimensional

structure via branching and cross-linking, increase the viscosity, and trigger the gelation process[58, 60]. Although the reactions occur at room temperature (RT), a subsequent heat treatment/calcination is required to obtain a crystallized product powder.
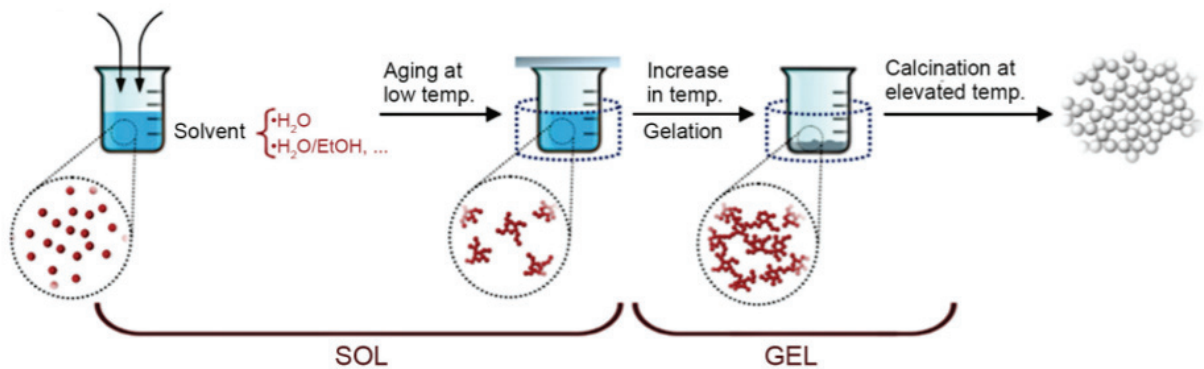
Figure 2.6. Sol-gel processing

(Source: Hashim, 2019)[59].

Sol-gel processing is advantageous because it provides high control of product composition and high purity. On the other hand, some drawbacks are limiting the use of the sol-gel method, such as hydrolysis rates of the reactants must be equal or close to synthesizing the desired product. Some difficulties also arise in controlling the particle morphology due to the uneven solvent removal. The heat treatment at elevated temperatures causes unavoidable agglomeration leading to inhomogeneous particle size distribution[46].

2.1.5 Coprecipitation Method

Coprecipitation is commonly used, faster than most other chemical methods, and suitable for production on the industrial scale[46, 56]. The schematical representation is given in Figure 2.7. First, a solution is prepared to contain the desired cations. With the addition of a precipitating agent or a ligand such as ammonia, potassium hydroxide, sodium

hydroxide or urea, etc., precipitation is induced. The precipitated product is isolated by filtration. A simple heat treatment process is then applied for transformation to the oxides via evaporation of the water or decomposition[60].
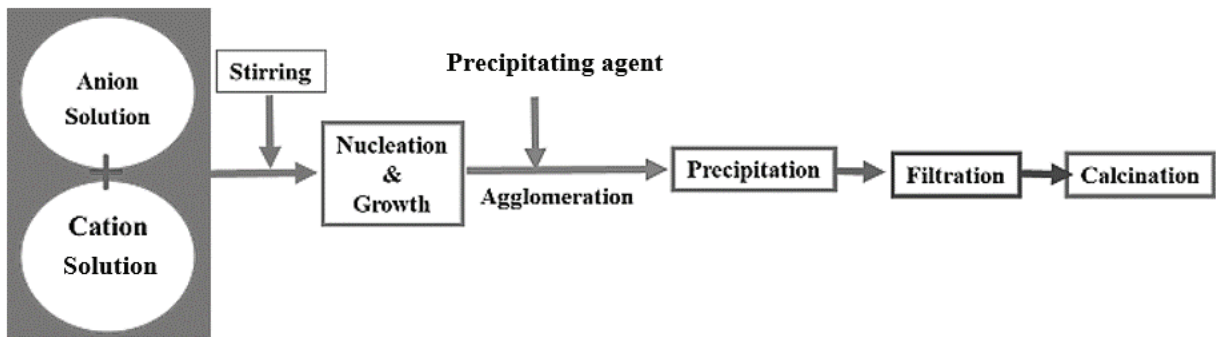
Figure 2.7. Coprecipitation synthesis

(Source: Venkatramana Reddy, 2019)[61].

The coprecipitation method has two key stages: nucleation with subsequent crystal growth. Right after the concentration of precursor atoms reaches the critical supersaturation, nucleation occurs. Such a stage is important from the engineering point of view. As summarized in Figure 2.8, nucleation speed has a great effect on particle size, such that fast nucleation yields small particles, and slow nucleation leads to bigger particles. To be able to control the kinetics of nucleation, it is needed to modify reaction conditions by changing the reaction temperature, environment, surfactant, etc[54]. During the growth stage, the solutes diffuse through the surface of the crystals, and product particles occur at this site[46].
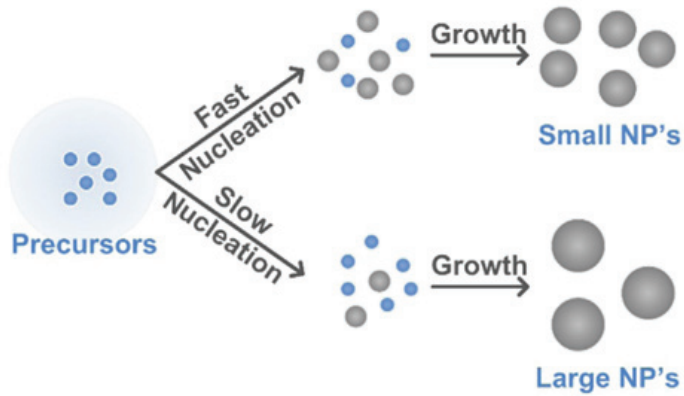
Figure 2.8. Crystal growth

(Source: Tailor,2020)[62].

The coprecipitation method can be considered beneficial since it provides good composition control and purity. However, due to the different precipitation and crystal growth rates, distorted homogeneity at the microscopic level and uncontrollable particle size distribution may arise[39]. Also, it is generally results in poorly crystallized intermediate products, including the mixture of hydrated oxides. In such a case, conversion to fully crystallized oxides by heat treatment becomes necessary[46].

2.1.6 Spray Pyrolysis

Flame spray pyrolysis is simply a one-step combustion process where the products are produced by thermal decomposition[58]. The precursor solution is broken into droplets by using an atomizer. It is sprayed directly into a flame where thermal decomposition resulting in the formation of the desired substance occurs and is collected on a substrate[54].

A visualization of the whole system is given in Figure 2.9. Mainly, the system consists of a self-sustaining, high-temperature flame for thermal decomposition, a substrate for particles to accumulate, a peristaltic pump to spray the solution, and a dispersion gas to carry the precursors[44, 58]. After the precursors were sprayed through the peristaltic pump, solvent evaporation occurs. The pyrolysis of the raw materials takes place, and they undergo thermal decomposition. Then, the product particles nucleate and

subsequently grow via agglomeration under the effect of high temperature[58, 63]. The flame is obtained by combustion of a fuel gas e.g., O_2 and the temperature may reach up to 3000°C, and its velocity changes between 80-100 m/s[63].
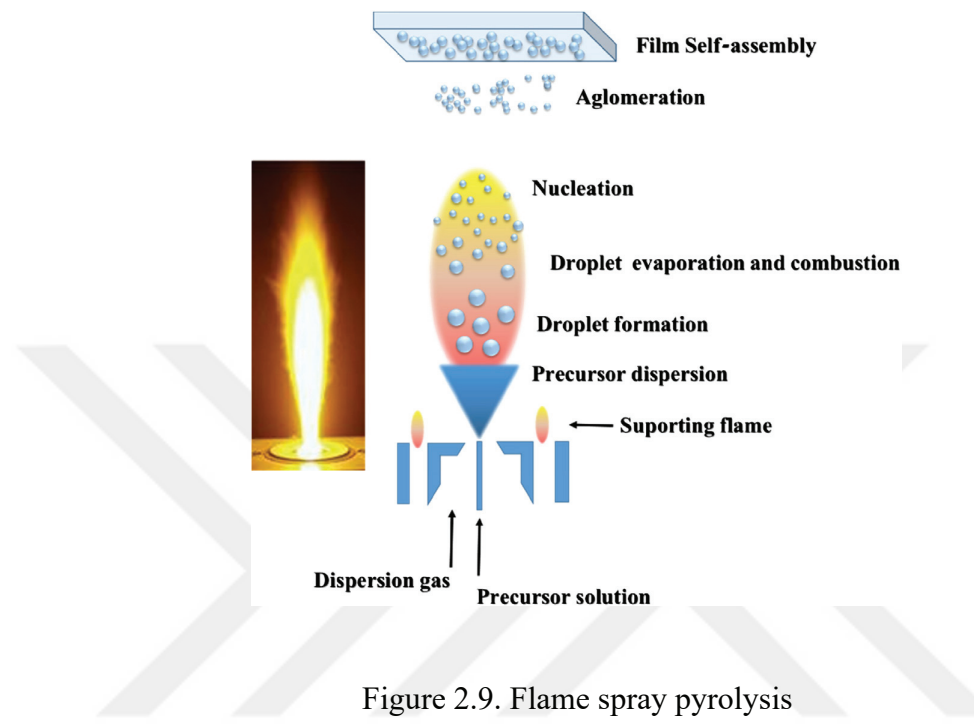
Figure 2.9. Flame spray pyrolysis

(Source: Nunes, 2019)[54].

Spray pyrolysis is preferred due to its proven scalability and ability to produce quite small particles, e.g., in the range of 5-500 nm[54]. On the other hand, it is hard to produce unagglomerated particles by this technique[64]. Moreover, there is a need for advanced separation processes to diminish the loss of products and environmental pollution. The process itself has already a high cost, and the cost becomes even higher with the sophisticated separation processes[65].

2.1.7 Hydro/solvothermal Reaction Method

The hydrothermal root merely consists of a heterogeneous reaction among the precursors in the presence of water as the solvent under controlled temperature and pressure. The method uses the solubility of most of the inorganic substances in aqueous mediums and subsequent crystallization of the product. However, the solubility of the raw materials in water may not be sufficient in some cases. Hence, various nonpolar solvents e.g., isopropanol, benzene, etc., can also be used instead of water. In such cases, the process is named solvothermal reaction. The process (hydro/solvothermal reaction) can be performed in two discrete ways: with or without a surfactant. Although the surfactant-free path can be considered as more economic, since it avoids the need for expensive surfactants, and simple, surfactants provide strong control on the morphology and growth behavior of the particles[56]. For instance, in the relevant studies[34, 66], dodecyl benzene sulfonate (SDBS) was used to transform the KNN-hydrate morphology with dodecahedra-shaped particles[67] to plate-like ones.

The process begins with the preparation of an aqueous solution containing desired cations at a specific concentration. After the addition of metal oxide powder precursor, the reaction is performed in a reactor or an autoclave (Figure 2.10(a)) under specified temperature and pressure. The filling ratio of the autoclave is generally adjusted within the range of $50 - 80$ vol%. According to the thermodynamic calculations, the reaction mixture becomes saturated, i.e., the hydrothermal conditions are reached, if the filling factor is higher than 32.6 vol% and the reaction temperature is above 100°C in the hydrothermal reaction system. Still, great caution is necessary for adjusting the reaction temperature and reactor filling ratio, because if the pressure generated within the reaction vessel, i.e., autogenous pressure, becomes too high, the risk of reactor explosion arises. To avoid such cases, the plot is given in Figure 2.10(b) is used, therefore the autogenous pressure within the autoclave may be predicted and the filling factor can be adjusted[68].
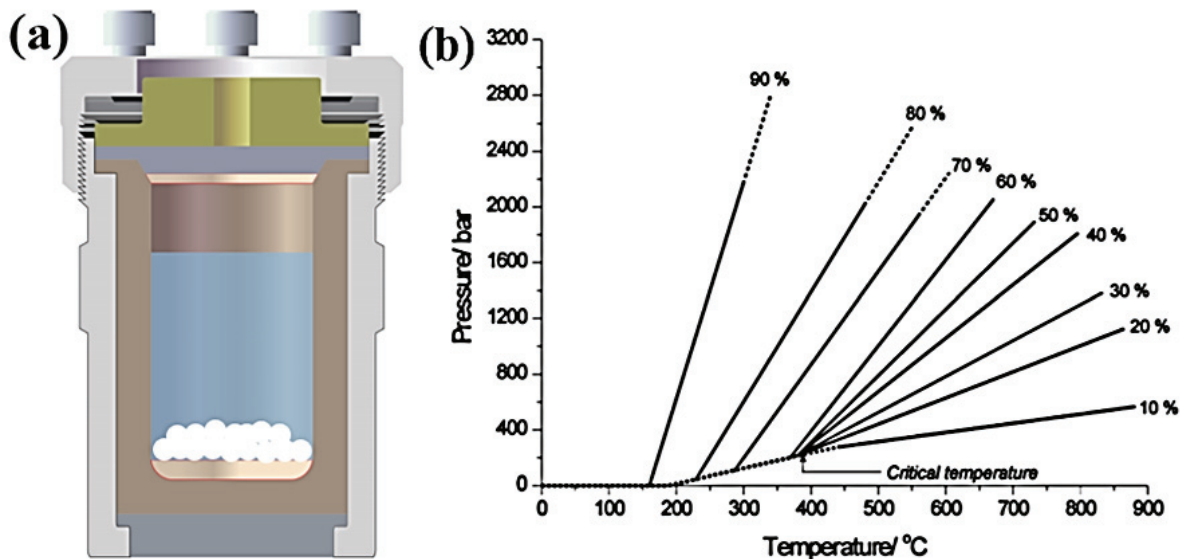
Figure 2.10. (a) Hydrothermal reaction autoclave; (b) Pressure dependence of water for different autoclave filling factors

(Source: Einarsrud, 2014)[68].

The hydrothermal method is favored mainly because the reaction temperatures are considerably lower compared to those of conventional methods. Generally speaking, this results in a more energy-saving and economical process[44]. In addition, hydrothermal differs from other low-temperature routes such as coprecipitation and sol-gel processing in the elimination of the calcination process in some cases. Besides all these, high purity products are obtained because there is no mixing process in a foreign medium, so the impurities are avoided[39]. Another outcome from the comparison of the hydrothermal method with other low-temperature routes is that the agglomeration rate is relatively low[44]. Also, there are narrow particle size distribution and molecular homogeneity among its advantages[56]. However, the drawbacks of the system include long reaction time and delicate reaction conditions which have to be carefully controlled to obtain the desired product[44].

CHAPTER 3

EXPERIMENTAL PROCEDURE

3.1 Materials

Niobium pentoxide, (Nb_2O_5, CAS#: 1212-96, 99.9%, Sigma Aldrich, USA) was used as the niobium source for potassium sodium niobate (KNN) powder synthesis via both solid-state and hydrothermal reaction. In conventional solid-state, carbonate salts (K_2CO_3, CAS#: 584-08-7, 99%, Sigma Aldrich, USA and Na_2CO_3, CAS#: 497-19-8, 99.5%, Sigma Aldrich, USA) were used as the alkali cation sources and ethanol, (EtOH, CAS#: 64-17-5, 100%, Merck, Germany) was used as the milling medium. On the other hand, in the hydrothermal route, hydroxide compounds (NaOH, CAS#: 1310-73-2, 98-100%, Sigma Aldrich, USA and KOH, CAS#: 1310-58-3, ≥86%, Sigma Aldrich, USA) were used as the sources for alkali cations. Deionized water (DI) (Ultrapure Type-I, 18.2 MΩ.cm at 25˚C) was the solvent and it was supplied by using a Millipak Direct-Q® 8 UV water purification system.

Apart from Nb_2O_5, ammonium niobate oxalate hydrate (ANO) ($C_4H_4NNbO_9 \cdot xH_2O$, 99.99%, Sigma Aldrich, USA) was also supplied as the niobium source only for the synthesis by sol-gel processing technique. The alkali cation sources were adjusted as sodium acetate ($C_2H_3NaO_2$, CAS#: 127-09-3, anhydrous, Merck, Germany) and potassium acetate ($C_2H_3KO_2$, CAS#: 127-08-2, extra pure, Merck, Germany). Finally, citric acid monohydrate ($C_6H_8O_7.H_2O$, CAS#: 5949-29-1, 99.5%, Merck, Germany) was used as the gelling agent and ethylene glycol was added to induce polymerization reaction.

3.2 Equipment

Retsch Planetary Ball Mill PM100 (see Figure 1.3 (a)) was used for the milling process using zirconia (ZrO2) balls. The calcination was carried out using an elevating oven (Protherm) in both solid-state reaction and sol-gel processing. The hydrothermal reaction was performed in stainless steel static autoclave (Parr instruments, model 4748 A acid digestion bomb, USA) visualized in Figure 1.12 (a). The reaction vessel was heated using a convection oven (Memmert, UN55, France). A digital hot plate (Weightlab, WN-H550) was used for the gelation process.

3.3. Synthesis via conventional solid-state reaction

Firstly, the precursor powders (Nb_2O_5, Na_2CO_3, and K_2CO_3) were weighed according to the stoichiometric ratio and ball milled in ethanol medium at 250 rpm for 24 h. After the slurry was dried, calcination was carried out at temperatures 700 - 900°C for 5 h dwell time. Then, the obtained powder was ground to avoid agglomeration caused by the treatment at elevated temperatures. The experimental set for the solid state reaction method is tabulated in Table 3.1.

Table 3.1. Experimental set for the conventional solid-state reaction

Code	Mole Ratio ($K_2CO_3:Na_2CO_3:Nb_2O_5$)	Milling Conditions	Milling Time and Temperature	Notes
SS1-700	1:1:2	24 s @ 250 rpm	5 h @ 700°C	5 mole% excess carbonates
SS2-750	1:1:2	24 s @ 250 rpm	5 h @ 750°C	5 mole% excess carbonates

SS3-800	1:1:2	24 s @ 250 rpm	5 h @ 800°C	5 mole% excess carbonates
SS4-850	1:1:2	24 s @ 250 rpm	5 h @ 850°C	-
SS5-900	1:1:2	24 s @ 250 rpm	5 h @ 900°C	5 mole% excess carbonates

3.4 Synthesis via hydrothermal reaction

As is Nb_2O_5 powder was initially subjected to ball milling at 250 rpm for 24 h in ethanol in order to decrease the average particle size. Then, an alkaline solution was prepared by dissolving cation sources, NaOH and KOH, in DI water. Total alkaline concentration and the ratio of K^+/Na^+ were varied in the range of 1-10 M and 1 - 10, respectively. Treated Nb_2O_5 was added into the hydroxide solution and stirred for 1 h to obtain a dispersion. The white suspension was sealed within stainless steel autoclave. To prevent corrosion due to the strongly basic medium, a Teflon reaction vessel was used with a filling factor of 70%. The autoclave was heated to 180-240°C for 3 - 24 h. In the end, the resultant powder was washed several times with DI water to obtain pH neutrality and filtrated by vacuum filtration. The filtrate dried at RT. The experimental set for hydrothermal synthesis is given in Table 3.2.

Table 3.2. Experimental set for the hydrothermal reaction

Code	K^+/Na^+ Ratio	Alkaline Concentration (M)	Temperature (˚C)	Time (h)
R#	1/2/4/8/10	6	200	24
OH#	6	1/2/4/6/8/10	200	24

Table 3.2. (cont.)

T#	6	6	160/180/200 /220/240	24
Rt#	6	6	200	4/8/15/24

3.5 Synthesis via sol-gel processing

Ammonium niobate oxalate monohydrate (ANO, $C_4H_4NNbO_9.H_2O$) was dissolved in 1 M citric acid (CA) solution by continuous stirring at 60°C for 20 mins. Simultaneously, 5 mmol of sodium and potassium acetates (dried at 150°C for 2 h) were dissolved in distilled water by adjusting the K^+/Na^+ ratio of 1 and 2. The acetate solution was added dropwise to the ANO-citric acid solution. Finally, 0.9 g of ethylene glycol (EG:CA=1.5) was added for the polymerization reaction. After 1 h of continuous mixing for complete dispersion, the gelation was performed at 100°C for 6 h with subsequent calcination in between 400 - 700°C with 100°C intervals. The experimental set for sol-gel processing is given in Table 3.3.

Table 3.3. Experimental set for sol-gel processing

Code	ANO (g)	K^+/Na^+ Ratio	CA Concentration (M)	Calcination Conditions
SG1	1.52	2	1	400°C for 5h
SG2	1.52	2	1	500°C for 5h
SG3	1.52	2	1	600°C for 5h
SG4	1.52	2	1	700°C for 5h

3.6 Characterization methods

Phase analyses were carried out using an XRD (Panalytical X'Pert PRO, The Netherlands) with a copper anode X-Ray source (Cu$_{K\alpha}$ = 1.5406 Å at 40kV, 30 mA). Scans were done between the 20° - 60° (2θ) range with 0.02° per second. Fourier Transform Infrared (FT-IR) spectra analysis (PerkinElmer, UATR Two, Waltham, MA, USA) was performed from 400 to 4000 cm^{-1} with 20 scans and 32 resolution. The morphology of the synthesized powders was analyzed by scanning electron microscopy (SEM, FEI Quanta 250 FEG, USA) using secondary electron (SE) mode, and size analyses were done in ethanol by a Malvern dynamic light scattering (DLS) Nano-ZS instrument (Worcestershire, UK). Thermal behaviors of the obtained powders were analyzed via thermogravimetric analysis (TGA, Netzsch STA 409, Netzsch Gerätebau Gmbh, Selb, Germany). The samples were heated from RT to 1200˚C with a 5˚C. min^{-1} heating rate in air.

CHAPTER 4

RESULTS AND DISCUSSION

4.1 KNN via Solid-state Synthesis

TG/DTA curves of the carbonate precursors are given in Figure 4.1. It appears that both powders had approximately 8% weight loss at around 100°C, indicating the absorbed moisture. Such a result supports the recorded hygroscopic nature of the potassium and sodium carbonate[5, 48, 50]. Hence, drying the carbonate precursors before the process becomes crucial to be able to perform stoichiometric weighing. Also, a second weight reduction represents the decomposition reaction starting at approximately above 800°C for Na_2CO_3 and K_2CO_3, respectively[69, 70]. Specifically, from the DTA curves appearing at 865°C as clear endothermic peaks for both carbonate salts.
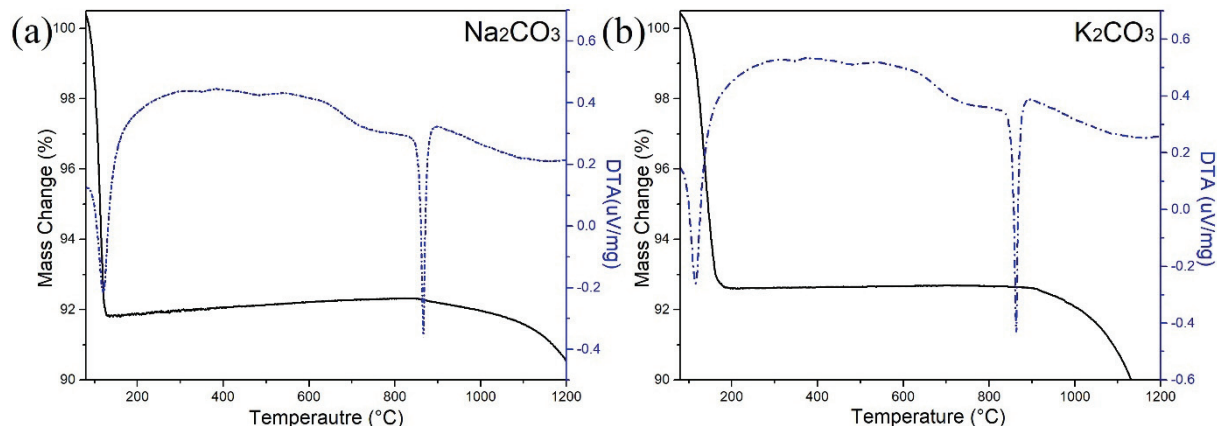
Figure 4.1. TG/DTA analysis of the carbonate precursors; (a) Na_2CO_3; (b) K_2CO_3

XRD patterns of the KNN powders synthesized at 850°C and the ICDD data of $K_{0.5}Na_{0.5}NbO_3$ (ICDD # 96-230-0500) are shown in Figure 4.2 (a). In addition to the orthorhombic $K_{0.5}Na_{0.5}NbO_3$, the second phase, $K_2Nb_8O_{21}$ (ICDD # 31-1060), was indexed for the SS – 850 sample. As mentioned in Section 1.1.1, the formation of such non-perovskite phases is attributed to the relatively high volatility of the alkali oxides at the corresponding (850°C) temperatures. Those may be varied, including $K_4Nb_6O_{17}$, $Na_2Nb_4O_{11}$, or $(K, Na)_2Nb_4O_{11}$, i.e., generally alkaline deficient compositions and are generally accepted as intermediate products[71, 72]. literature, the addition of excess alkali precursors was purposed to prevent alkali losses during calcination and eliminate the formation of impurity phases[13, 23, 48]. Therefore, the experiment was repeated (SS – 850 – R) with 5 mol% excess carbonate precursors, and phase pure orthorhombic KNN phase was obtained.

KNN synthesis was also performed at different calcination temperatures varying from 700 to 900°C, and XRD analyses are given in Figure 4.2 (b). It is seen that phase pure orthorhombic KNN synthesis was accomplished at all covered temperatures. Still, it is worth mentioning the increased sharpness of the peaks as the reaction was carried out at higher temperatures. Hence, it might be said that better crystallinity was obtained at elevated processing temperatures.
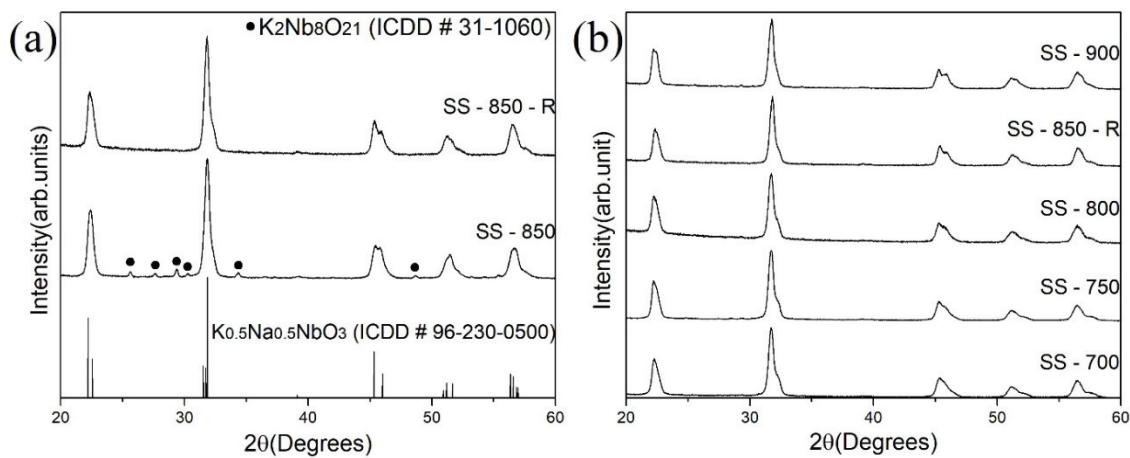
Figure 4.2. XRD patterns of (a) ICDD data of K0.5Na0.5NbO3 and KNN powders synthesized via solid-state reaction at 850°C with (SS – 850 – R) and without (SS – 850) using excess carbonate precursors; (b) KNN powders synthesized

via solid-state reaction at 700°C (SS – 700), 750°C (SS – 750), 800°C (SS – 800), 850°C (SS – 850 – R) and 900°C (SS – 900) calcination temperatures.

SEM images of the SS – 850 – R coded sample are given in Figure 4.3. As indicated in the experimental procedure (Section 3.3), the powders were subjected to the final grinding after the calcination process to avoid particle agglomeration. Figure 4.3 (a) demonstrates the produced particles before the final grounding stage to observe particle growth. Micron scaled (2 – 5 μm) cubic KNN particles are clearly seen. Such growth has been reported for KNN structures[73-75]. Although the particles became having irregular shapes after the post-grounding step, a significant particle size reduction was observed from above 5 microns to 382 ± 69 nm. DLS plot of the sample is given in Figure 4.3 (c).
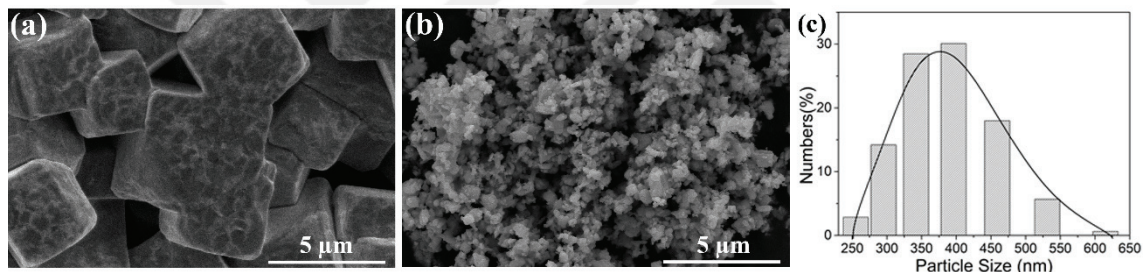
Figure 4.3. Analysis of KNN powders synthesized at 850°C by solid-state reaction, SEM images (a) before; (b) after the grinding; (c) DLS data.

4.2 KNN via Hydrothermal Synthesis

While anhydrous Nb2O5 was commonly used for KNN synthesis, it is known to be having quite low water solubility[76], which leads to reduced dissolution and reaction rates. Here, as is Nb_2O_5 was initially ball-milled to decrease the particle size and increase reactivity[77]. In the end, the particle size of the commercial powder was reduced from 450 nm to 250 nm, as demonstrated in DLS analyses given in Figure 4.4.
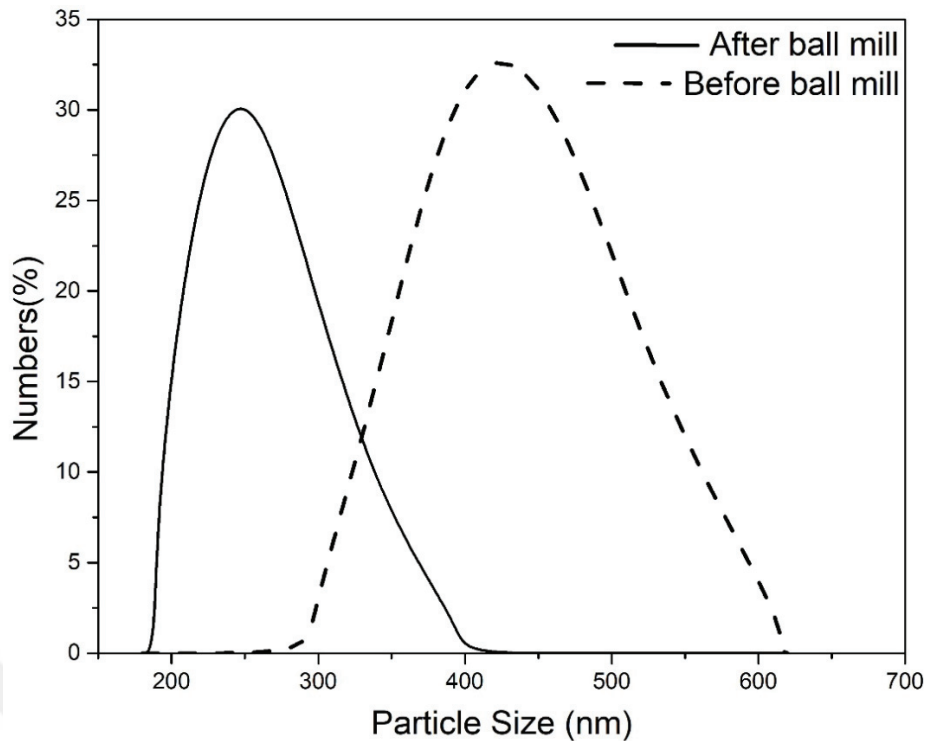
Figure 4.4. DLS analysis of commercial (dashed line) and ball milled (solid line) Nb_2O_5.

4.2.1 Effect of K^+/Na^+ Ratio

The alkali cation ratio (K^+/Na^+) was altered within the range of $1 - 10$ while keeping the total hydroxide concentration at 6M and reaction temperature at 200°C for 24 h to study the influences on the final product. XRD data of the powders are demonstrated in Figure 4.5 with the ICDD data of three distinctive niobate phases, $NaNbO_3$ (ICDD # 96-101-1065), $K_{0.5}Na_{0.5}NbO_3$ (ICDD # 96-230-0500), and $KNbO_3$ (96-231-0012) to underline the peak shifts. When the cation ratio was adjusted to 1,2, and 4 (HT – R1, HT – R2, and HT – R4), the patterns were resolved for the pure $NaNbO_3$ phase. Such a result probably originates from the reported higher reaction rate between sodium and niobium than the rate between potassium and niobium[32, 77]. Also, take notice that the diffusivity of potassium ions is lower than the sodium ions[78].

Defining the exact stoichiometric composition of the KNN phase is quite challenging for the reason of being a solid solution. However, it could be said that the

pattern of the sample HT – R6, indicates the orthorhombic K-rich (x>0.5) $K_xNa_{1-x}NbO_3$ phase if the shift towards lower 2θ angles compared to $K_{0.5}Na_{0.5}NbO_3$ ICDD data is realized. Since the radius of the potassium ion (1.33 Å) is larger than that of sodium (0.95 Å), enhanced interplanar spacing results in decreased diffraction angles according to Bragg's Law[79-81]. The presence of the $NaNbO_3$ phase kept within the system as a secondary phase, see the shoulder corresponding to 30.5° (2θ), which is a problem also observed in the relevant work[67]. Keep in mind the lower Gibbs free energy of $NaNbO_3$ formation reaction (-59 J.mol^{-1}) compared to the $KNbO_3$ (-49 J.mol^{-1}), indicating that $NaNbO_3$ formation is thermodynamically more favorable[82]. When the alkali ratio was further increased to 8 (HT – R8) and 10 (HT – R10), the pattern approached $KNbO_3$ ICDD data pointing to further incorporation of potassium ions within the crystal lattice.
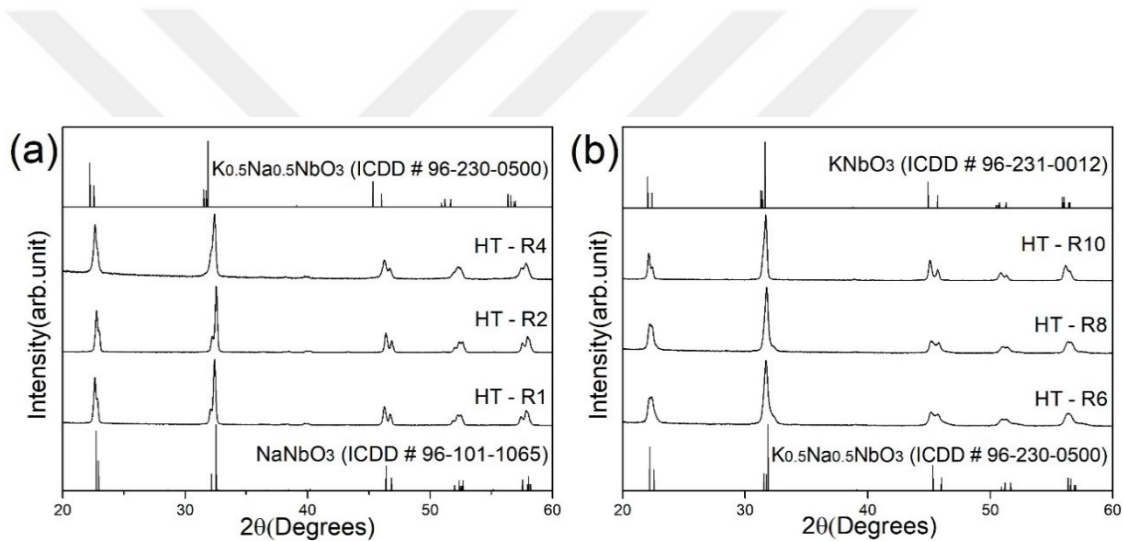
Figure 4.5. ICDD patterns of $K_xNa_{1-x}NbO_3$ ($0 \leq x \leq 1$) and XRD analysis of samples obtained at 200°C for 24 h by reacting the alkaline solution of total 6 M total alkaline concentration with K^+/Na^+ ratio of; (a) 1 (HT – R1), 2 (HT – R2) and 4 (HT – R4); (b) 6 (HT – R6), 8 (HT – R8) and 10 (HT – R10).

The quantitative results obtained by Rietveld refinement are tabulated in Table 4.1. Overall, the data support the XRD outcomes. All of the samples had K-rich stoichiometry. While the sodium occupancy (1-x) is 0.16 ($K_{0.84}Na_{0.16}NbO_3$), when the cation ratio is adjusted to 6, it decreases to smaller values than 0.05 ($K_{0.95}Na_{0.05}NbO_3$ and

$K_{0.99}Na_{0.01}NbO_3$) for higher ratios. As it would be expected, increased K^+/Na^+ ratio resulted in more potassium ions accumulated within the lattice.

Table 4 1. Quantitative results of KNN samples obtained at 200°C for 24 h by reacting the alkaline solution of the total 6 M total alkaline concentration with the K^+/Na^+ ratio of 6 (HT – R6), 8 (HT – R8), and 10 (HT – R10).

Sample	R_{wp}	$NaNbO_3$ phase (%vol)	$K_xNa_{1-x}NbO_3$ Phase (%vol)	Na occupancy, (1-x)
HT-R6	0.1122	9.67	90.33	0.16
HT-R8	0.1433	-	100	0.01
HT-R10	0.1766	-	100	0.04

The morphology of the sample R1 (K^+/Na^+) is demonstrated in Figure 4.6 and rectangular prismatic particles agree well with the literature[83, 84]. Also, a bimodal particle size distribution is clearly seen with approximately 200-300 nm particles, and relatively larger ones, approximately 800-1000 nm. When the cation ratio was increased to 4 (see Figure 4.6 (b)), distortion in the shape of those prismatic particles was observed with some additional cube-like particles. Such an observation, in fact, might be a hint for KNN formation. In Figure 4.6(c), the cubic morphology is seen with particles 250 – 350 nm in size, representing the KNN phase. Somehow, when the cation ratio was reached to 8 and finally 10, the sharp edges of the cubic particles disappeared as reported in the previous studies[32, 80].
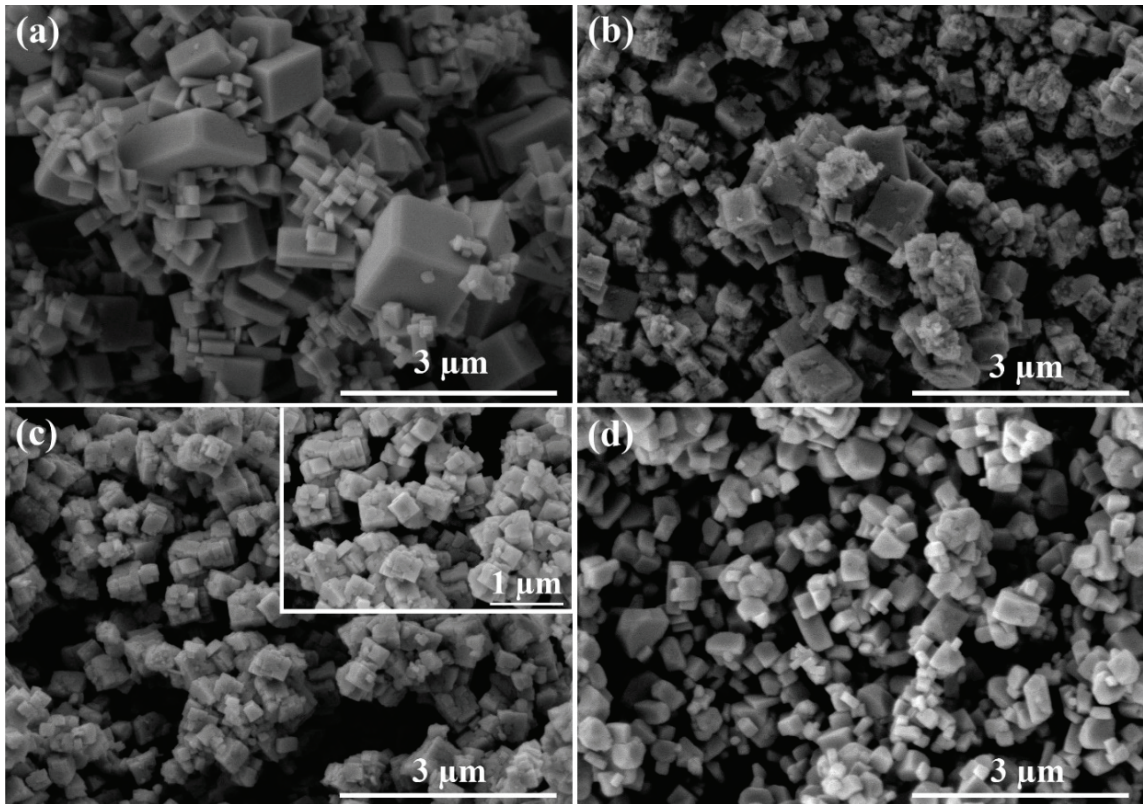
Figure 4.6. SEM images of samples by reaction under 6 M total hydroxide concentration at 200°C for 24 h (a) $K^+/Na^+=1$, (b) $K^+/Na^+=4$, (c) $K^+/Na^+=6$ (the upper-right inset shows magnified image), (d) $K^+/Na^+=10$.

4.2.2 Effect of Alkaline Concentration

The total alkaline concentration was altered within the range of $1 - 10$ M while keeping other the cation ratio, reaction temperature, and time at 6, 200°C and 24 h, respectively, to observe alkalinity level effects on the system. In Figure 4.7 (a), the XRD data of the samples are visualized. Under 1 M alkaline concentration (OH1), the pattern indexed for the Nb_2O_5, phase indicated that the alkalinity level was not sufficient to solve the niobium precursor within 24 h. Increased alkalinity is known to be promoting hydrolysis reaction of Nb_2O_5 which is essential for KNN formation[36]. As the alkaline concentration was reached up to first 2 M and then 4 M, the pattern resolved for the same phase, which was sodium-potassium hexaniobate, $K_4Na_4Nb_6O_{19}.9H_2O$ (PDF# 00-014-

0360). Actually, such a phase has been reported in the previous works as the intermediate product of hydrothermally KNN synthesis and named as KNN – hydrate ($K_xNa_{8-x}Nb_6O_{19}.nH_2O$)[67, 81, 85, 86]. It can be said that the minimum alkalinity limit to form a perovskite structure is 6 M. KNN synthesis under presenting conditions according to the XRD data of the sample OH6, OH8, and OH10, the coexistence of K-rich KNN and $NaNbO_3$ was observed in each set.

The morphology of the powder obtained under 4 M total alkaline concentration is shown in Figure 3.7(b). Dodecahedra-shaped[67] particles with around 1 μm sizes indicate the hexaniobate structure, as found out by XRD analyses in Figure 4.7. (a). On the other hand, the morphology evolved to cube-like particles (see Figure 4.6 (c)) as the total alkalinity was increased to 6 M. The relatively larger dodecahedral hexaniobate particles were replaced with smaller (250 – 350 nm) cubic particles via dissolution-precipitation mechanism[67, 85]. Further increase in the total alkaline concentration, reaching 10 M, was resulted in the observation of micron-sized aggregates with cubic shapes in Figure 4.7 (d). Such growth was conceptually called the oriented attachment[87], which has been observed in KNN structures, as well[85, 88]. In the growth via oriented attachment, first, the random particle collision occurs originating from the Brownian motion. Subsequently, those find the configuration with the lowest energy by orientation[87]. In fact, reduction of the surface energy is the driving force of the mechanism[89], and it is accomplished by the elimination of collision surfaces and aggregation[87]. A schematic representation of the growth behavior is given in Figure 4.7 (e).
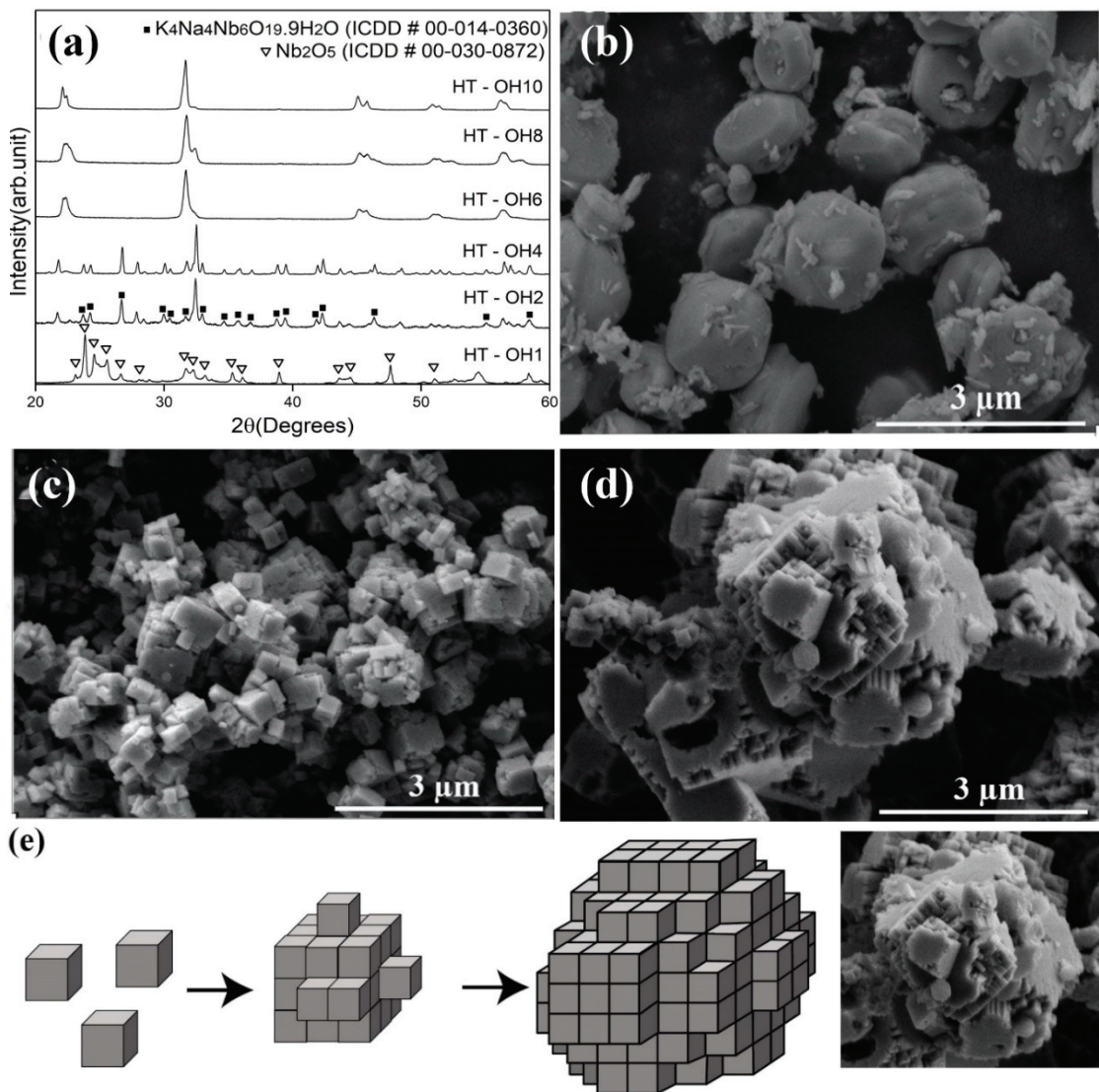
Figure 4.7. XRD analysis of samples obtained varied alkaline concentrations; [OH⁻]=1-10 M (OH 1- 10) reacted with the solution having $K^+/Na^+=6$ at 200°C for 24 h; and SEM images of those samples (b) [OH⁻]=4, (c) [OH⁻]=8 M, and (d) [OH⁻]=10 M, (e) schematic representation regarding the growth behavior of KNN crystals.

4.2.3 Effect of Reaction Time

The reaction kinetics were investigated under both 6 M and 8 M total alkaline concentration with constant reaction temperature (200°C) and cation ratio ($K^+/Na^+=6$).

XRD patterns of the obtained powders under 6 M are given in Figure 4.8 (a). The intermediate product, i.e., the mixed hexaniobate phase, was resolved for the first 8 h of the reaction (see the dodecahedra-shaped hexaniobate morphology in Figure 4.8 (b&c)). Also, it is worth mentioning a second morphology, apart from hexaniobate is seen at the eighth hour of the reaction under 6 M alkaline concentration (Figure 4.8 (c)). The phase is constituted by much smaller (approximately 100 nm) particles relative to dodecahedral hexaniobate and represents the initiation of KNN crystals precipitation, presumedly. Such co-existence was also observed in Figure 4.7(b), after 24 h of reaction of the same solution under 4 M. After 15 h of reaction, the transformation of those structures to cube-like KNN crystals was completed in Figure 4.8 (d).
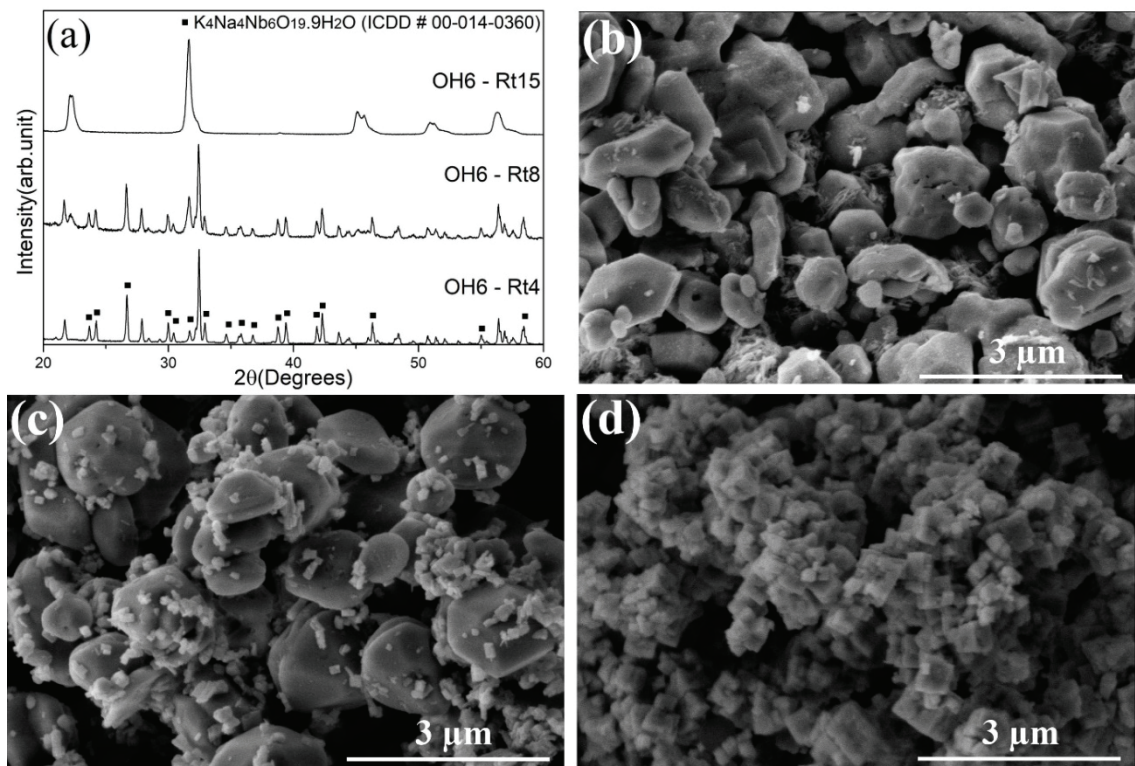
Figure 4.8. XRD analysis of samples obtained varied reaction times; 4 h (OH6 – Rt4), 8 h (OH6 – Rt8) and 15 h (OH6 – Rt15) under 6 M total alkaline concentration with K^+/Na^+=6 at 200°C for 24 h; and SEM images of those samples (b) OH6 – Rt4, (c) OH6 – Rt8, and (d) OH6 – Rt15.

XRD analysis of the powders synthesized under 8 M is given in Figure 4.9 (a). It appeared that the required reaction time for perovskite KNN formation is only 6 h under 8 M total alkaline concentration (see the cubic KNN morphology in Figure 4.9 (c)). Keep in mind that while conversion of the mixed hexaniobate to orthorhombic KNN was observed within 15 h under 6 M, it is not even been accomplished within 24 h under 4 M total alkalinity (see Figure 4.7 (a)). Those are strong indications that the reaction operates faster as the alkalinity level increases. Also, take notice of the increased particle size in the cube-like morphology under 8 M alkalinity when the reaction proceeds first to 12 h (Figure 4.9(c)) then 24 h (Figure 4.7(c)). Apparently, once the KNN cubes precipitated, the growth of the crystals got involved via the oriented attachment, as discussed in Section 4.2.1.
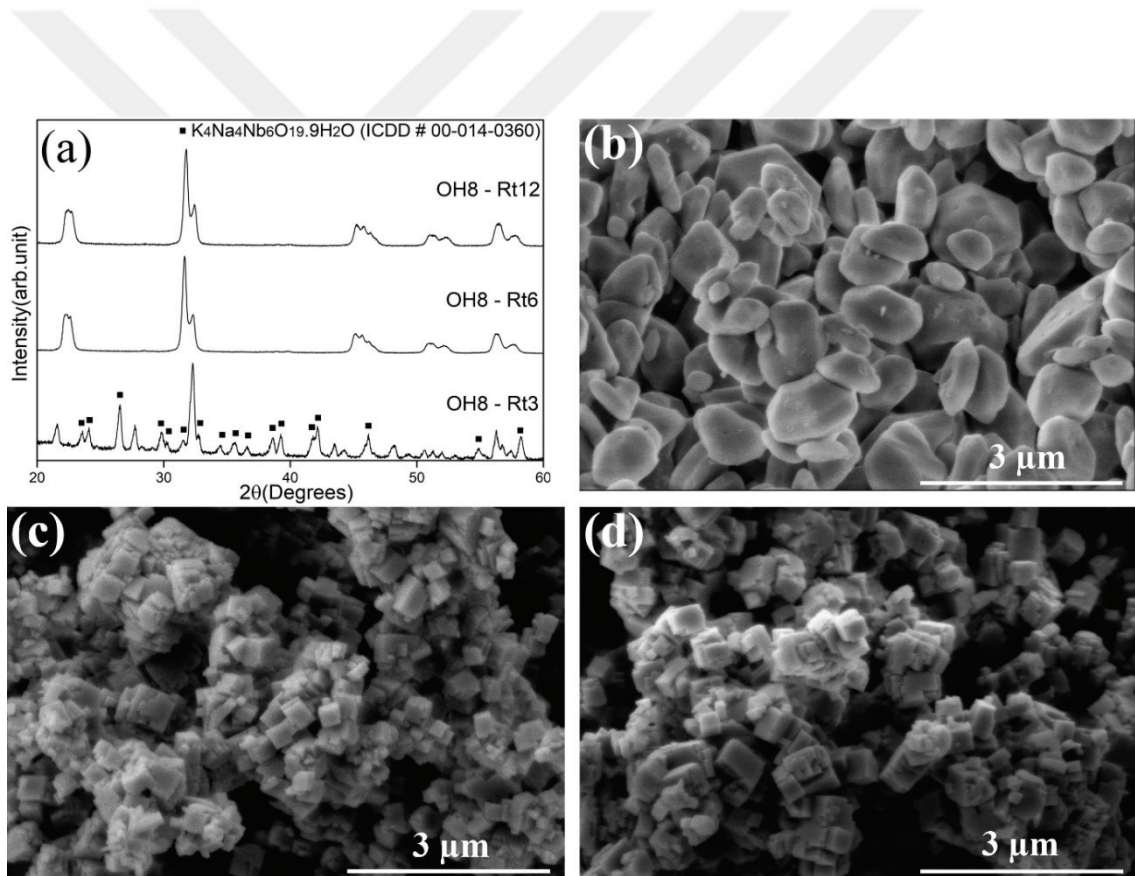
Figure 4.9. (a) XRD analysis of samples obtained varied reaction times; 3 h (OH8 – Rt3), 6 h (OH8 – Rt6) and 12 h (OH8 – Rt12) under 8 M total alkaline concentration with K^+/Na^+=6 at 200°C for 24 h; and SEM images of those samples (b) OH8 – Rt3, (c) OH8 – Rt6, and (d) OH8 – Rt12.

The FTIR spectra of the powders synthesized with the alkali ratio of 6 under 6 M hydroxide concentration at 200°C for 4, 8, and 15 h of reactions are given in Figure 4.10. The signals corresponding to 4 and 8 h of reaction consist of two identical peaks in between 3500-2500 cm^{-1} and at around 1600 cm^{-1}. The peak corresponding to 3500-2500 cm^{-1} range is attributed to [OH$^-$] group, and the latter (1600 cm^{-1}) indicates, on the other hand, chemically bonded, i.e., absorbed water molecules, that are indicated by n (K$_x$Na$_{8-x}$Nb$_6$O$_{19}$.nH$_2$O), in the hexaniobate structure[35, 90, 91]. At the fourth hour of the reaction, five clear split peaks, marked by arrows, were observed in the 1000 – 500 cm^{-1} band to declare the presence of the Lindqvist hexaniobate structure[92, 93]. As the reaction time was increased to 15 h, the peak at 1600 cm^{-1} disappeared, which was expected since the hydrated hexaniobates were not found in the powder (see Figure 4.9(a)). In addition, it appeared that the split peaks in between 1000 – 500 cm^{-1} became one relatively broad peak corresponding to the same wavenumbers for the 15 h reaction. In fact, the one broad peak is correlated with NbO$_6$ octahedrons[35, 94] and the perovskite structure[90, 91]. On the other hand, the broad signal (3500-2500 cm^{-1}) representing the [OH$^-$] group is still visible even after 15 h, which is common in the literature for hydrothermally synthesized samples without post-annealing at temperatures below 550°C[35, 91].
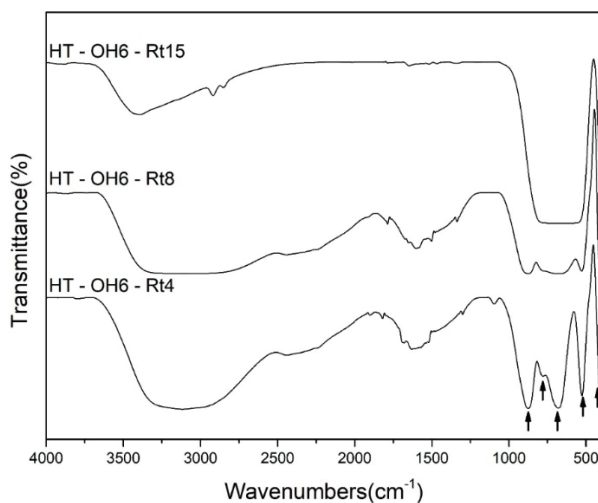
Figure 4.10. FTIR spectra of powders obtained with the alkaline ratio of 6 under 6 M alkaline concentration at 200°C for 4 (HT – Rt4), 8 (HT – Rt8), and 15 h (HT – Rt15) of reaction.

4.2.4 Effect of Reaction Temperature

For reaction temperature investigation, the synthesis reaction was carried out at varying temperatures; 160, 180, 200, 220, and 240°C under 6 M total alkalinity with $K^+/Na^+=6$ at 200°C for 24 h. XRD analysis of each set is given in Figure 4.11 (a), and it is seen that formation of the orthorhombic KNN was not accomplished below 200°C. It is known that reaction temperature has a major effect on the size of the final particles[95-97]. According to the DLS analysis given in Figure 3.11 (b), while the average particle size was 368 nm ∓ 45 nm at 200°C, it was increased to first 445 ∓ 69 nm at 220°C and then 525 ∓ 97 nm at 240°C. The size distribution was also affected and expanded to wider ranges when the reaction was carried out at higher temperatures. Hexaniobate morphology constituted by dodecahedra-shaped micron-sized particles was observed for reactions at 160 and 180°C (see Figure 3411 (c&d)). Above 200°C, sub-micron cubic KNN particles were observed (see Figure 4.6 (c)), and the morphology was maintained despite further temperature increase (Figure 4.11 (e&f)).
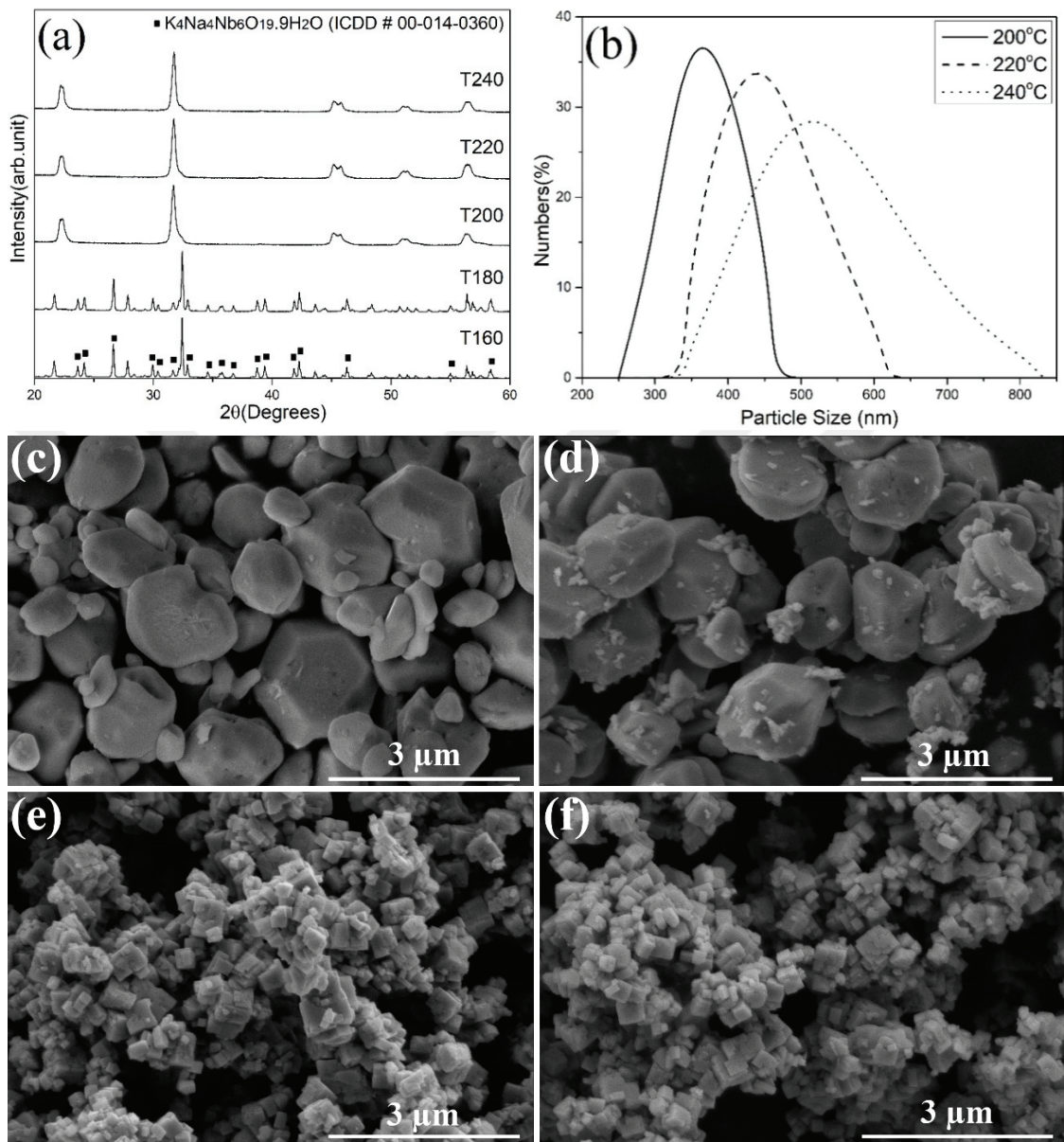
Figure 4.11. Analysis of powders obtained with $K^+/Na^+=6$ under 6 M total alkaline concentration for 24 h at 160 (T160), 180 (T180), 200(T200), 220 (T220) and 240°C(T240) (a) XRD; (b) DLS plot of T200, T220 and T240; SEM images of (c) T160; (d) T180; (e) T220; (f) T240.

4.2.5 Probable Formation Mechanisms

There have been several studies in the literature regarding the reaction mechanism of KNN formation[80-82, 85, 88, 98]. However, there are some inconsistencies among the proposed routes, such as the intermediate mixed hexaniobate product has been ignored in some of the works[82, 85, 98], while it has been underlined in a few others[67, 77, 80, 81, 88, 99]. The formation mechanism is schematically demonstrated in Figure 4.12. First, Nb_2O_5 dissolves into the hexaniobate ion $Nb_6O_{19}^{8-}$ (Lindqvist ion), consisting of six edge-sharing NbO_6 octahedra, in the high alkaline medium through Eqn. (I)[85, 100, 101]. Nevertheless, the Lindqvist ion is known to be unstable at higher pH and temperature[101]. Hence, $Nb_6O_{19}^{8-}$ ion might be transformed to varied end-products, such as if the medium consists of K^+ ions $K_8Nb_6O_{19}.13H_2O$ and/or $KNbO_3$ forms[101-103]. Instead, $HNa_7Nb_6O_{19}.13H_2O$ and/or $NaNbO_3$ may be obtained with the existence of Na^+ ions[102, 104]. In other respects, if there is a co-existence of both K^+ and Na^+ ions, the mixed hexaniobate (KNN-hydrate) e.g., layered $K_xNa_{8-x}Nb_6O_{19}.9H_2O$ phase, forms through the dissolution-crystallization mechanism (see Eqn. II) if the required reaction conditions are met[67, 105]. This phase is composed of one water layer between two (K, Na) NbO_3 oxygen octahedron layers (see Figure 4.12). Subsequently, primary KNN crystals nucleates via dissolution-recrystallization (or reprecipitation) mechanism[67, 77, 85, 86, 88, 103, 105].

$$3Nb_2O_5 + 8OH^- \rightarrow Nb_6O_{19}^{8-} + 4H_2O \tag{I}$$

$$Nb_6O_{19}^{8-} + (8 - 8x)K^+ + 8xNa^+ + nH_2O \rightarrow K_{8-8x}Na_{8x}Nb_6O_{19}.nH_2O, \tag{II}$$

$$K_{8-8x}Na_{8x}Nb_6O_{19}.nH_2O \rightarrow 6K_{1-x}Na_xNbO_3 + (2 - 2x)K^+ + (2x)Na^+ + 2OH^-$$
$$+ (n - 1)H_2O \tag{III}$$
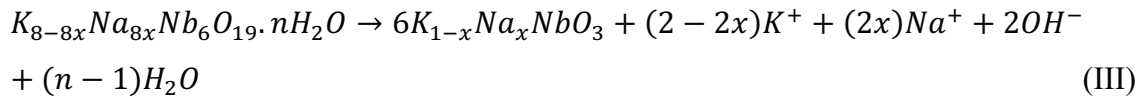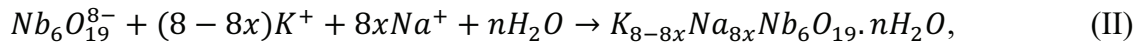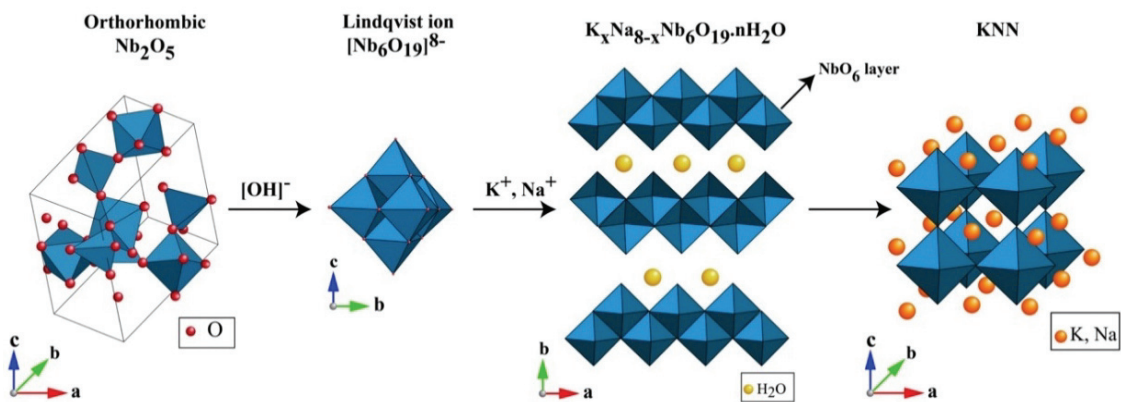
Figure 4.12. Schematic representation of KNN formation mechanism via hydrothermal reaction

(Source: Gu, 2017; Magrez, 2006)[105, 106].

4.2.6 Hydrothermal Reaction with Post-Heat Treatment

The hydrothermally synthesized biphasic KNN powder composing of $K_{0.84}Na_{0.16}NbO_3$ (90.33 vol%) and $NaNbO_3$ (9.67 vol%) phases, as tabulated in Table 4.1, was subjected to a post-heat treatment at 800°C for 2 h. The XRD pattern of the sample, before and after the process, is given in Figure 3.13. Somehow, a peak shift towards higher angles, see the upper-right inset for the 30.5 - 33° 2θ range, was observed after the post-annealing. In addition to the consumption of the second $NaNbO_3$ phase, the shift implies the increased sodium occupancy within the crystal lattice. The quantitative result of the heat-treated powder is given in Table 4.2.

Table 4.2. Quantitative results of the post-heat treated sample.

Sample	R_{wp}	NaNbO$_3$ phase (%vol)	$K_xNa_{1-x}NbO_3$ Phase (%vol)	Na occupancy, (1-x)
R6 @ 800°C	0.1520	-	100.00	0.42

It appears that the post-heat treatment process induced the sodium incorporation into the lattice, stoichiometry became $K_{0.58}Na_{0.42}NbO_3$ and the composition approached the MPB composition (x=0.50) significantly in agreement with the relevant works[67, 88].
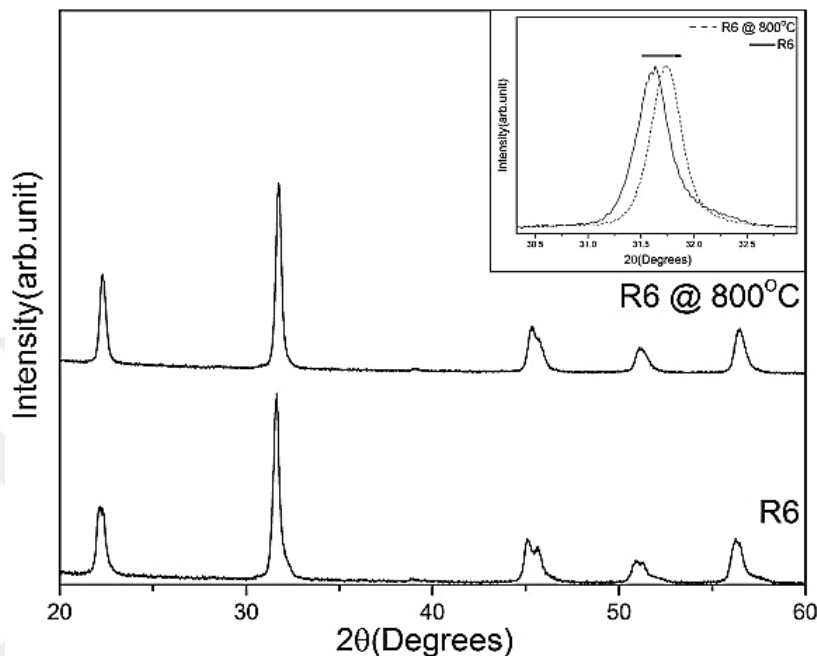
Figure 4.13. XRD pattern of the KNN powder obtained with K^+/Na^+=6 under 6 M alkaline concentration at 200°C for 24 h before and after the post-heat treatment, the inset shows the magnified section of 30.5-33° (2θ) range.

4.2.7 Compositional Survey

In addition to the investigated parameters, compositional surveys (see Figure 4.14) were constructed using the quantitative data obtained using the Rietveld refinements. The refinements were employed over 65 samples by systematically altering the total hydroxide concentration between 2 - 10 M, alkaline ratio (K^+/Na^+); 2 - 10, and reaction temperature; 160°C - 240°C. The obtained phases were classified under four groups: (I) Hexaniobate ($(K,Na)Nb_6O_{19}{}^{8-}$), (II) Sodium niobate ($NaNbO_3$), (III) biphasic system: $NaNbO_3$ + K-rich (x > 0.5) KNN, and (IV) phase-pure K-rich (x > 0.5) KNN.

It is seen from Figure 4.14 that increased reaction temperature, total hydroxide concentration, and alkaline ratio resulted in decreased $NaNbO_3$ phase fraction and promoted K-rich KNN formation. Also, higher total hydroxide concentration facilitated the perovskite formation at lower temperatures. Among all the samples the maximum proximity to the MPB composition was obtained by the reaction with a K^+/Na^+ ratio of 6 under 4 M alkaline concentration at 240°C for 24 h, and the composition was $K_{0.54}Na_{0.46}NbO_3$. However, this phase only constituted the 30.01 vol% of the sample, and the rest was the $NaNbO_3$ phase.
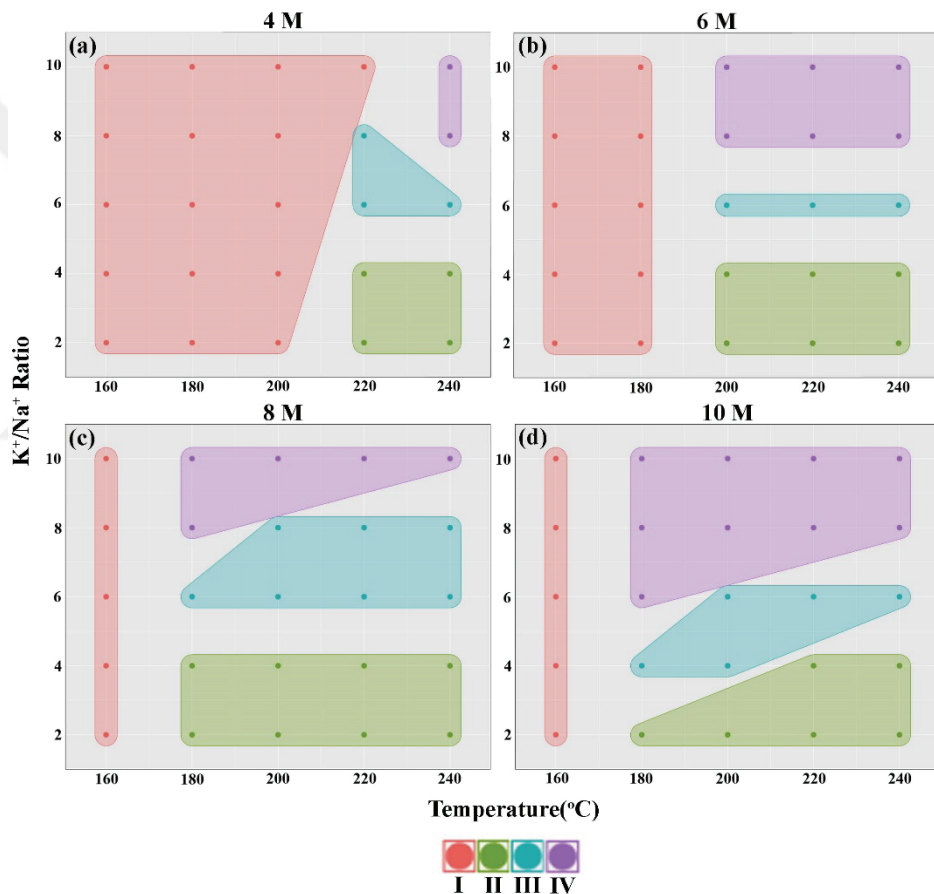
Figure 4.14. The visualizations were made in R Statistical Software using the ggplot and the ggforce packages. The convex hulls surrounding the points were generated with the following configuration 'geom_mark_hull(concavity = 5, expand = unit(10, "mm"), radius = unit(10,"mm"))'. The data points were extracted from the Rietveld refinements performed over the XRD data of the samples obtained under the total hydroxide concentration of **(a)** 4 M; **(b)** 6

M; **(c)** 8 M; and **(d)** 10 M, with varied alkaline ratio (K^+/Na^+) and reaction temperature. The color scale bar shows the codes for the observed phases; I: Hexaniobate, II: single-phase $NaNbO_3$ (NN), III: Consolidated biphasic compositions (NN + $K_xNa_{1-x}NbO_3$, KNN (x > 0.5), and IV: Single phase KNN (x > 0.7).

4.3 KNN via Sol-gel Processing

Sol-gel synthesis of KNN was carried out at varied calcination temperatures including, 400, 500, 600, and 700°C. According to the XRD patterns given in Figure 4.14(a), the powder is primarily amorphous at 400°C, despite visible KNN structure peaks with low intensities. Hence, a complete crystal structure could not be obtained at such a temperature. When the temperature was adjusted to 500°C and above, the peaks were resolved for the perovskite potassium-rich KNN structure. On the other hand, an impurity phase was identified as potassium bicarbonate (Kalicinite, $KHCO_3$ (ICDD # 01-070-1167). It has been proposed in the previous works that KNN powders have a hygroscopic nature[107, 108] and a high tendency to react with CO_2 in ambient air upon storage[109, 110]. It may originate from the potassium and/or sodium species that remained within the system after the synthesis[107]. Consequently, carbonate impurities were observed, such as in the current work. Although the synthesized powders were stored at 100°C to avoid moisture and decelerate carbonate formation, complete elimination was not possible, which was expected considering the period when the samples stand in ambient air before and during the XRD analysis. Accordingly, it is best to store KNN powders under an inert atmosphere. Also, as the calcination temperature was increased, the particle size increased (see DLS analysis in Figure 4.14(b)) from 145.5 ± 17 nm to first 314.7 ± 40 nm (from 500°C to 600°C) and then 482.5 ± 84 nm at 700°C.
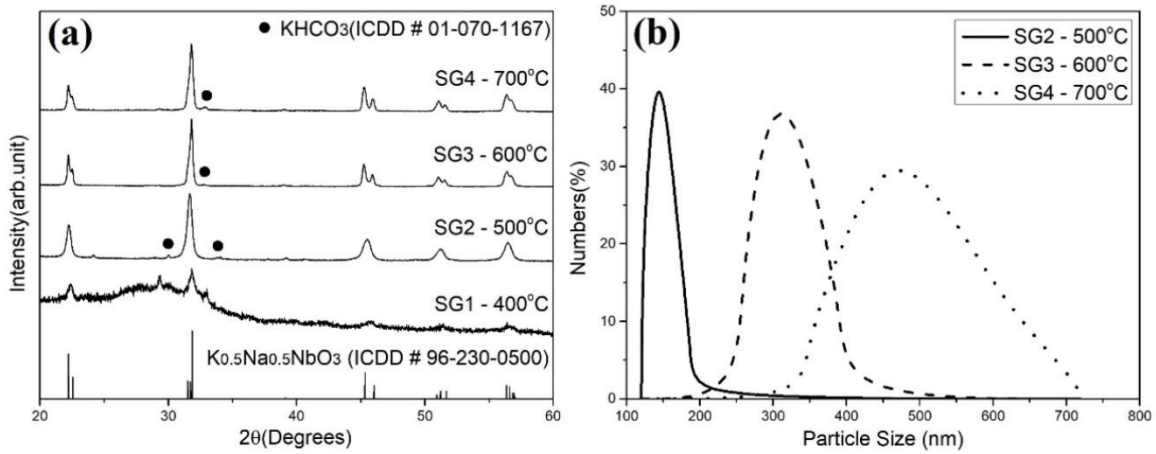
Figure 4.15. Analysis of powders obtained via sol-gel method at varied calcination temperatures (a) XRD; (b) DLS.

SEM images of the KNN powders calcined at altered temperatures are demonstrated in Figure 4.15. At 400°C, the powder was constituted by mostly ellipse-like particles having about 1 μm in size. Note that the morphology was inhomogeneous and also contained smaller spherical particles. As the calcination temperature was increased, first, the cube-like KNN morphology with ~ 150 nm particle size was observed at 500°C, which is consistent with the XRD patterns in Figure 4.14(a). Further increase to 700°C resulted in larger grains (482.5 ± 84 nm, see Figure 4.14(b)) with more homogeneous particle size distribution, in agreement with the resembling works[28, 29, 111, 112].
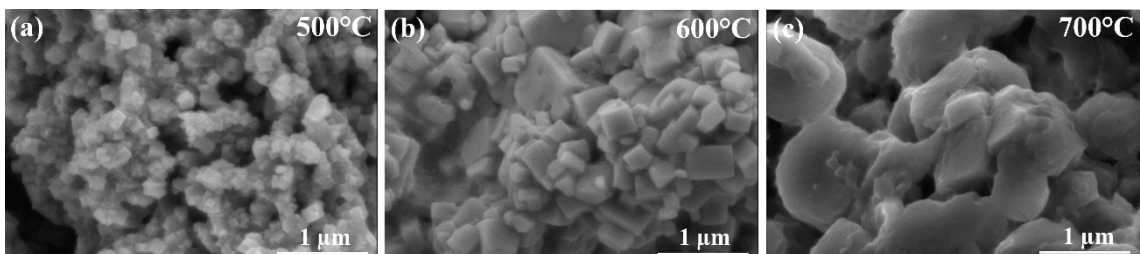
Figure 4.16. SEM images of powders obtained via sol-gel method at varied calcination temperatures (a) 500°C; (b) 600°C; (c) 700°C.

CHAPTER 5

CONCLUSIONS

In this thesis, for the first time, a comprehensive comparative study was employed to obtain $K_xNa_{1-x}NbO_3$ powders using three distinct methods: solid-state reaction, hydrothermal synthesis, and sol-gel processing. The samples were characterized in depth, both morphologically and structurally.

In the conventional solid-state synthesis, according to the XRD analysis, the phase pure $K_{0.5}Na_{0.5}NbO_3$ powder having 382 ± 68 nm particle size was obtained by calcination conducted at 850°C. The main problem with the method was that the relatively high volatility of the alkaline components (Na_2O and K_2O) led to uneven volatilization of the species at those temperatures, and, eventually, non-perovskite impurity phases ($K_2Nb_8O_{21}$, $Na_2Nb_4O_{11}$, etc.) formed. Although excess precursors were used to avoiding such problems, it was quite challenging to balance the stoichiometry and obtain the $K_{0.5}Na_{0.5}NbO_3$ phase without any impurities.

In the hydrothermal reaction, the studied parameters consisted of total alkaline concentration, cation (K^+/Na^+) ratio, reaction time, and temperature. The results demonstrated that for perovskite structure formation, at least 6 M total alkaline concentration was needed during 24 h reaction at 200°C. Below those conditions, the mixed hexaniobate ($K_xNa_{8-x}Nb_6O_{19}.nH_2O$) phase, which is the intermediate product of the KNN formation mechanism, was obtained. Such phase was constituted by the dodecahedra-shaped particles which were, then replaced with cubic KNN crystals via the dissolution-precipitation mechanism. According to the morphological changes, those crystals probably grew via the oriented attachment. In this mechanism, the primary particles randomly collided upon, Brownian motion and the particle-particle interfaces were eliminated by the aggregation to reduce the surface energy. In the end, relatively larger crystals were formed by coalescing smaller ones. The increased alkalinity level accelerated the reaction according to the kinetic study. Finally, the temperature increase (from 200°C to 240°C) yielded the particle size increased from 368 nm $\pm$ 45 nm to 525 ± 97 nm.

An important point regarding hydrothermally KNN synthesis is that since sodium atoms react faster with niobium atoms than potassium atoms, the formation of solid solution KNN could not be accomplished for the cation ratios below 6. Instead, the formation of single-phase $NaNbO_3$ was observed according to the quantitative results. Unfortunately, it was challenging to control the stoichiometry and to obtain single-phase $K_{0.5}Na_{0.5}NbO_3$ powder by hydrothermal reaction. However, when the hydrothermally obtained K-rich KNN powder having the secondary $NaNbO_3$ phase was post-treated at 800°C, not only $NaNbO_3$ was consumed, but also the sodium ions were incorporated within the crystal lattice and generate a single-phase KNN approaching the MPB composition.

In the sol-gel processing method, the crystalline KNN structure was obtained at 500°C with 145.5 ± 17 nm particle size. The calcination temperature was increased up to 700°C with 100°C intervals. As a result, the particle size of the synthesized powders increased first to 314.7 ± 40 nm at 600°C and then 482.5 ± 84 nm at 700°C. Nevertheless, the samples were contaminated by the reaction of KNN with CO_2 in ambient air during storage. In that case, the necessity for KNN powders, obtained via the sol-gel route, to be stored at inert conditions arises.

In conclusion, the main objective should be maintaining the stoichiometry at the morphotropic phase boundary (MPB), i.e., $x \sim 0.5$, where the maximum piezoelectric performance was obtained. Unfortunately, obtaining the exact MPB composition seems challenging for all studied methods. For both conventional and sol-gel synthesis, the precursors, alkali carbonates and acetates, respectively, have hygroscopic nature. Such an issue may probably be the cause of stoichiometric deviations. Also, in the conventional synthesis, alkali oxide volatilization is another problem. Although hydrothermal reaction offered the least control over the stoichiometry, post-heat treatment of the hydrothermally synthesized biphasic (KNN and $NaNbO_3$) powder was appeared as the best alternative to obtain single-phase $K_{0.5}Na_{0.5}NbO_3$.

REFERENCES

1.   Hao, J.; Li, W.; Zhai, J.; Chen, H., Progress in high-strain perovskite piezoelectric ceramics. *Materials Science and Engineering: R: Reports* **2019,** *135*, 1-57.

2.   Uchino, K., The development of piezoelectric materials and the new perspective. In *Advanced Piezoelectric Materials*, Elsevier: 2017; pp 1-92.

3.   Zheng, T.; Wu, J.; Xiao, D.; Zhu, J., Recent development in lead-free perovskite piezoelectric bulk materials. *Progress in materials science* **2018,** *98*, 552-624.

4.   Malič, B.; Koruza, J.; Hreščak, J.; Bernard, J.; Wang, K.; Fisher, J. G.; Benčan, A., Sintering of lead-free piezoelectric sodium potassium niobate ceramics. *Materials* **2015,** *8* (12), 8117-8146.

5.   Hagh, N. M.; Jadidian, B.; Safari, A., Property-processing relationship in lead-free (K, Na, Li) NbO 3-solid solution system. *Journal of Electroceramics* **2007,** *18* (3-4), 339-346.

6.   Rödel, J.; Jo, W.; Seifert, K. T.; Anton, E. M.; Granzow, T.; Damjanovic, D., Perspective on the development of lead-free piezoceramics. *Journal of the American Ceramic Society* **2009,** *92* (6), 1153-1177.

7.   Directive, E. W. R., 19/EU of the European Parliament and of the council of on waste electrical and electronic equipment (WEEE). Off. *J. Eur. Union* **2003**.

8.   Directive, E.; RoHS, I., Restriction of the Use of Certain Hazardous Substances in Electrical and Electronic Equipment. *European Union, Brussels, Belgium, Report* **2010,** (A7-0196).

9.   Bhalla, A.; Guo, R.; Roy, R., The perovskite structure—a review of its role in ceramic science and technology. *Materials research innovations* **2000,** *4* (1), 3-26.

10.   Haertling, G. H., Ferroelectric ceramics: history and technology. *Journal of the American Ceramic Society* **1999,** *82* (4), 797-818.

11.   Jaffe, B.; Roth, R.; Marzullo, S., Piezoelectric properties of lead zirconate-lead titanate solid-solution ceramics. *Journal of Applied Physics* **1954,** *25* (6), 809-810.

12.   Wu, J.; Xiao, D.; Zhu, J., Potassium–sodium niobate lead-free piezoelectric materials: past, present, and future of phase boundaries. *Chemical reviews* **2015,** *115* (7), 2559-2595.

13.   Egerton, L.; Dillon, D. M., Piezoelectric and dielectric properties of ceramics in the system potassium—sodium niobate. *Journal of the American Ceramic Society* **1959,** *42* (9), 438-442.

14.   López-Juárez, R.; González, F.; Villafuerte-Castrejón, M.-E., Lead-free ferroelectric ceramics with perovskite structure. *Ferroelectrics-Material Aspects* **2011,** *5* (1), 305-330.

15.   Tellier, J.; Malic, B.; Dkhil, B.; Jenko, D.; Cilensek, J.; Kosec, M., Crystal structure and phase transitions of sodium potassium niobate perovskites. *Solid State Sciences* **2009,** *11* (2), 320-324.

16.   Saito, Y.; Takao, H.; Tani, T.; Nonoyama, T.; Takatori, K.; Homma, T.; Nagaya, T.; Nakamura, M., Lead-free piezoceramics. *Nature* **2004,** *432* (7013), 84-87.

17.   Tressler, J. F.; Alkoy, S.; Newnham, R. E., Piezoelectric sensors and sensor materials. *Journal of electroceramics* **1998,** *2* (4), 257-272.

18.   Li, P.; Zhai, J.; Shen, B.; Zhang, S.; Li, X.; Zhu, F.; Zhang, X., Ultrahigh piezoelectric properties in textured (K, Na) NbO3-based lead-free ceramics. *Advanced materials* **2018,** *30* (8), 1705171.

19.   Jaeger, R.; Egerton, L., Hot pressing of potassium-sodium niobates. *Journal of the American Ceramic Society* **1962,** *45* (5), 209-213.

20.   Matsubara, M.; Yamaguchi, T.; Kikuta, K.; Hirano, S.-i., Sinterability and piezoelectric properties of (K, Na) NbO3 ceramics with novel sintering aid. *Japanese Journal of Applied Physics* **2004,** *43* (10R), 7159.

21.   Guo, Y.; Kakimoto, K.-i.; Ohsato, H., Phase transitional behavior and piezoelectric properties of (Na 0.5 K 0.5) Nb O 3–Li Nb O 3 ceramics. *Applied physics letters* **2004,** *85* (18), 4121-4123.

22.   Zuo, R.; Fang, X.; Ye, C., Phase structures and electrical properties of new lead-free (Na 0.5 K 0.5) Nb O 3–(Bi 0.5 Na 0.5) Ti O 3 ceramics. *Applied Physics Letters* **2007,** *90* (9), 092904.

23.   Safari, A.; Hejazi, M., Lead-free KNN-based piezoelectric materials. In *Lead-Free Piezoelectrics*, Springer: 2012; pp 139-175.

24.   Zeng, J.; Kwok, K. W.; Chan, H., KxNa1− xNbO3 powder synthesized by molten-salt process. *Materials Letters* **2007,** *61* (2), 409-411.

25.   Cheng, L.-Q.; Wang, K.; Li, J.-F., Synthesis of highly piezoelectric lead-free (K, Na) NbO 3 one-dimensional perovskite nanostructures. *Chemical Communications* **2013,** *49* (38), 4003-4005.

26.   Rahman, A.; Cho, K. H.; Ahn, C. W.; Ryu, J.; Choi, J. J.; Kim, J. W.; Yoon, W. H.; Choi, J. H.; Park, D. S.; Hahn, B. D., Seed crystal of modified potassium sodium niobate prepared by simple molten salt synthesis. *Journal of the American Ceramic Society* **2018,** *101* (2), 515-519.

27.   Fang, J.; Wang, X.; Li, L., Properties of Ultrafine-Grained Na0. 5K0. 5NbO3 Ceramics Prepared From Nanopowder. *Journal of the American Ceramic Society* **2011,** *94* (6), 1654-1656.

28.   Khorrami, G. H.; Kompany, A.; Zak, A. K., A facile sol–gel approach to synthesize KNN nanoparticles at low temperature. *Materials Letters* **2013,** *110*, 172-175.

29.   Zhang, D.-Q.; Qin, Z.-C.; Yang, X.-Y.; Zhu, H.-B.; Cao, M.-S., Study on synthesis and evolution of sodium potassium niobate ceramic powders by an oxalic acid-based sol–gel method. *Journal of sol-gel science and technology* **2011,** *57* (1), 31-35.

30.   Kumar, P.; Pattanaik, M., Synthesis and characterizations of KNN ferroelectric ceramics near 50/50 MPB. *Ceramics International* **2013,** *39* (1), 65-69.

31.   Haugen, A. B.; Madaro, F.; Bjørkeng, L.-P.; Grande, T.; Einarsrud, M.-A., Sintering of sub-micron K0. 5Na0. 5NbO3 powders fabricated by spray pyrolysis. *Journal of the European Ceramic Society* **2015,** *35* (5), 1449-1457.

32.   Zhang, F.; Han, L.; Bai, S.; Sun, T.; Karaki, T.; Adachi, M., Hydrothermal synthesis of (K, Na) NbO3 particles. *Japanese Journal of Applied Physics* **2008,** *47* (9S), 7685.

33.   Bai, L.; Zhu, K.; Su, L.; Qiu, J.; Ji, H., Synthesis of (K, Na) NbO3 particles by high temperature mixing method under hydrothermal conditions. *Materials Letters* **2010,** *64* (1), 77-79.

34.   Bai, S.; Karaki, T., Two-step Synthesis of Platelike Potassium Sodium Niobate Template Particles by Hydrothermal Method. *Journal of the American Ceramic Society* **2013,** *96* (8), 2515-2518.

35.   Zhang, D.; Cheng, Z.; Cheng, J.; Shi, F.; Yang, X.; Zheng, G.; Cao, M., Hydrothermal preparation and characterization of sheet-like (KxNa1− x) NbO3 perovskites. *Ceramics International* **2016,** *42* (7), 9073-9078.

36.   Ramajo, L. A.; Rubio-Marcos, F.; Del Campo, A.; Fernández, J. F.; Castro, M. S.; Parra, R., New insights into the properties of KxNa (1− x) NbO3 ceramics obtained by hydrothermal synthesis. *Ceramics International* **2014,** *40* (9), 14701-14712.

37.   Li, L.; Gong, Y.-Q.; Gong, L.-J.; Dong, H.; Yi, X.-F.; Zheng, X.-J., Low-temperature hydro/solvothermal synthesis of Ta-modified K0. 5Na0. 5NbO3 powders and piezoelectric properties of corresponding ceramics. *Materials & Design* **2012,** *33*, 362-366.

38.   Gu, Q.; Zhu, K.; Liu, J.; Wang, J.; Qiu, J.; Cao, Y.; Liu, P.; Yao, L., Solvothermal synthesis and formation mechanism of potassium sodium niobate mesocrystals under low alkaline conditions. *Journal of nanoscience and nanotechnology* **2015,** *15* (7), 4934-4940.

39.   Cousin, P.; Ross, R., Preparation of mixed oxides: a review. *Materials Science and Engineering: A* **1990,** *130* (1), 119-125.

40.   Shin, H.; Lee, S.; Jung, H. S.; Kim, J.-B., Effect of ball size and powder loading on the milling efficiency of a laboratory-scale wet ball mill. *Ceramics International* **2013,** *39* (8), 8963-8968.

41.   Malič, B.; Kuščer, D.; Vrabelj, M.; Koruza, J., Review of methods for powder-based processing. *Magnetic, ferroelectric, and multiferroic metal oxides* **2018**, 95-120.

42.   Feizpour, M.; Ebadzadeh, T.; Jenko, D., Synthesis and characterization of lead-free piezoelectric (K0. 50Na0. 50) NbO3 powder produced at lower calcination temperatures: A comparative study with a calcination temperature of 850° C. *Journal of the European Ceramic Society* **2016,** *36* (7), 1595-1603.

43.   Nandini, R. N.; Krishna, M.; Suresh, A.; Murthy, H. N., Effect of MWCNTs on piezoelectric and ferroelectric properties of KNN composites. *Materials Science and Engineering: B* **2018,** *231*, 40-56.

44.   Segal, D., Chemical synthesis of ceramic materials. *Journal of Materials Chemistry* **1997,** *7* (8), 1297-1305.

45.   Athayde, D. D.; Souza, D. F.; Silva, A. M.; Vasconcelos, D.; Nunes, E. H.; da Costa, J. C. D.; Vasconcelos, W. L., Review of perovskite ceramic synthesis and membrane preparation methods. *Ceramics International* **2016,** *42* (6), 6555-6571.

46.   Stojanovic, B. D.; Dzunuzovic, A. S.; Ilic, N. I., Review of methods for the preparation of magnetic metal oxides. In *Magnetic, Ferroelectric, and Multiferroic Metal Oxides*, Elsevier: 2018; pp 333-359.

47.   Uchino, K., Manufacturing methods for piezoelectric ceramic materials. In *Advanced Piezoelectric Materials*, Elsevier: 2017; pp 385-421.

48.   Kosec, M.; Malič, B.; Benĉan, A.; Rojac, T., KNN-based piezoelectric ceramics. In *Piezoelectric and Acoustic Materials for Transducer Applications*, Springer: 2008; pp 81-102.

49.   Wang, Y.; Damjanovic, D.; Klein, N.; Setter, N., High-temperature instability of Li-and Ta-modified (K, Na) NbO3 piezoceramics. *Journal of the American Ceramic Society* **2008,** *91* (6), 1962-1970.

50.   Kosec, M.; Maliĉ, B.; Benĉan, A.; Rojac, T.; Tellier, J., Alkaline niobate-based piezoceramics: crystal structure, synthesis, sintering and microstructure. *Functional materials letters* **2010,** *3* (01), 15-18.

51.   Suryanarayana, C.; Ivanov, E., Mechanochemical synthesis of nanocrystalline metal powders. In *Advances in powder metallurgy*, Elsevier: 2013; pp 42-68.

52.   Xu, C.; De, S.; Balu, A. M.; Ojeda, M.; Luque, R., Mechanochemical synthesis of advanced nanomaterials for catalytic applications. *Chemical communications* **2015,** *51* (31), 6698-6713.

53.   Ambika, S.; Devasena, M.; Nambi, I. M., Synthesis, characterization and performance of high energy ball milled meso-scale zero valent iron in Fenton reaction. *Journal of environmental management* **2016,** *181*, 847-855.

54.   Nunes, D.; Pimentel, A.; Santos, L.; Barquinha, P.; Pereira, L.; Fortunato, E.; Martins, R., Synthesis, design, and morphology of metal oxide nanostructures. *Metal Oxide Nanostructures* **2019**, 21-57.

55.   Sikalidis, C., *Advances in ceramics: synthesis and characterization, processing and specific applications*. BoD–Books on Demand: 2011.

56.   Malwal, D.; Packirisamy, G., Recent advances in the synthesis of metal oxide (MO) nanostructures. *Synthesis of Inorganic Nanomaterials* **2018**, 255-281.

57.   Liu, P.; Heinson, W. R.; Sorensen, C. M.; Chakrabarty, R. K., Kinetics of sol-to-gel transition in irreversible particulate systems. *Journal of colloid and interface science* **2019,** *550*, 57-63.

58.   Dhand, C.; Dwivedi, N.; Loh, X. J.; Ying, A. N. J.; Verma, N. K.; Beuerman, R. W.; Lakshminarayanan, R.; Ramakrishna, S., Methods and strategies for the synthesis of diverse nanoparticles and their applications: a comprehensive overview. *Rsc Advances* **2015,** *5* (127), 105003-105037.

59.   Hashim, N. C.; Frankel, D.; Nordin, D., Graphene oxide-modified hydroxyapatite nanocomposites in biomedical applications: A review. *Ceramics-Silikaty* **2019**.

60.   Bernier, J., Chemical processing for electronic ceramics: a challenge. *Materials Science and Engineering: A* **1989,** *109*, 233-241.

61.   Venkatramana Reddy, S.; Peyyala, S., Synthesis And Characterization of Al Doped And (Co, Al) co-doped ZnO Nanoparticles via Chemical co-precipitation Method. *Asian Journal of Nanosciences and Materials* **2019,** *2* (1), 111-119.

62.   Tailor, N. K.; Satapathi, S., The impact of Cs3Bi2Cl9 single crystal growth modality on its symmetry and morphology. *Journal of Materials Research and Technology* **2020,** *9* (4), 7149-7157.

63.   Pawłowski, L., Application of solution precursor spray techniques to obtain ceramic films and coatings. *Future Development of Thermal Spray Coatings* **2015**, 123-141.

64.   Kammler, H. K.; Mädler, L.; Pratsinis, S. E., Flame synthesis of nanoparticles. *Chemical Engineering & Technology: Industrial Chemistry-Plant Equipment-Process Engineering-Biotechnology* **2001,** *24* (6), 583-596.

65.   Snyders, C. D.; Ferg, E. E.; Schuelein, J.; Loewe, H., A review of using spray pyrolysis through sol-gel materials in the synthesis of cathode materials for lithium-ion batteries. *South African Journal of Chemistry* **2016,** *69*, 88-97.

66.   Bai, S.; Wen, Y.; Zhang, F.; Karaki, T.; Adachi, M., Influence of hydrothermal conditions on size of template particles for textured ceramics. *Japanese Journal of Applied Physics* **2011,** *50* (1S2), 01BE17.

67.   Handoko, A. D.; Goh, G. K., Hydrothermal synthesis of sodium potassium niobate solid solutions at 200° C. *Green Chemistry* **2010,** *12* (4), 680-687.

68.   Einarsrud, M.-A.; Grande, T., 1D oxide nanostructures from chemical solutions. *Chemical Society Reviews* **2014,** *43* (7), 2187-2199.

69.   Newkirk, A.; Aliferis, I., Drying and decomposition of sodium carbonate. *Analytical chemistry* **1958,** *30* (5), 982-984.

70.   Sabzevari, M.; Sajjadi, S. A.; Moloodi, A., Physical and mechanical properties of porous copper nanocomposite produced by powder metallurgy. *Advanced Powder Technology* **2016,** *27* (1), 105-111.

71.   Thong, H.-C.; Payne, A.; Li, J.-W.; Jones, J. L.; Wang, K., The origin of chemical inhomogeneity in lead-free potassium sodium niobate ceramic: Competitive chemical reaction during solid-state synthesis. *Acta Materialia* **2021,** *211*, 116833.

72.   Malic, B.; Jenko, D.; Holc, J.; Hrovat, M.; Kosec, M., Synthesis of sodium potassium niobate: A diffusion couples study. *Journal of the American Ceramic Society* **2008,** *91* (6), 1916-1922.

73.   Thong, H.-C.; Zhao, C.; Zhu, Z.-X.; Chen, X.; Li, J.-F.; Wang, K., The impact of chemical heterogeneity in lead-free (K, Na) NbO3 piezoelectric perovskite: Ferroelectric phase coexistence. *Acta Materialia* **2019,** *166*, 551-559.

74.   Wu, L.; Zhang, J.; Wang, C.; Li, J., Influence of compositional ratio K/Na on physical properties in (K x Na 1− x) NbO 3 ceramics. *Journal of Applied Physics* **2008,** *103* (8), 084116.

75.   Villafuerte-Castrejón, M. E.; Morán, E.; Reyes-Montero, A.; Vivar-Ocampo, R.; Peña-Jiménez, J.-A.; Rea-López, S.-O.; Pardo, L., Towards lead-free piezoceramics: Facing a synthesis challenge. *Materials* **2016,** *9* (1), 21.

76.   Deblonde, G. J.-P.; Chagnes, A.; Bélair, S.; Cote, G., Solubility of niobium (V) and tantalum (V) under mild alkaline conditions. *Hydrometallurgy* **2015,** *156*, 99-106.

77.   Park, S.; Peddigari, M.; Kim, J. H.; Kim, E.; Hwang, G.-T.; Kim, J.-W.; Ahn, C.-W.; Choi, J.-J.; Hahn, B.-D.; Choi, J.-H., Selective phase control of dopant-free potassium sodium niobate perovskites in solution. *Inorganic chemistry* **2020,** *59* (5), 3042-3052.

78.   Lin, T.-H.; Yund, R., Potassium and sodium self-diffusion in alkali feldspar. *Contributions to Mineralogy and Petrology* **1972,** *34* (3), 177-184.

79.   Biggin, P.; Smith, G.; Shrivastava, I.; Choe, S.; Sansom, M., Potassium and sodium ions in a potassium channel studied by molecular dynamics simulations. *Biochimica et Biophysica Acta (BBA)-Biomembranes* **2001,** *1510* (1-2), 1-9.

80.   Lv, J. H.; Zhang, M.; Guo, M.; Li, W. C.; Wang, X. D., Hydrothermal synthesis and characterization of KxNa (1− x) NbO3 powders. *International Journal of Applied Ceramic Technology* **2007,** *4* (6), 571-577.

81.   Zhang, M.; Guo, M.; Zhou, Y., Low-Temperature Preparation of KxNa (1− x) NbO3 Lead-Free Piezoelectric Powders by Microwave-Hydrothermal Synthesis. *International Journal of Applied Ceramic Technology* **2011,** *8* (3), 591-596.

82.   Zhang, C.; Haijun, L.; Min, G.; Zhang, M.; Xidong, W., Thermodynamic evaluation and hydrothermal preparation of KxNa1− xNbO3. *Rare Metals* **2008,** *27* (4), 371-377.

83.   Song, H.; Ma, W., Hydrothermal synthesis of submicron NaNbO3 powders. *Ceramics International* **2011,** *37* (3), 877-882.

84. Li, G.; Kako, T.; Wang, D.; Zou, Z.; Ye, J., Synthesis and enhanced photocatalytic activity of NaNbO3 prepared by hydrothermal and polymerized complex methods. *Journal of Physics and Chemistry of Solids* **2008,** *69* (10), 2487-2491.

85. Wang, Z.; Gu, H.; Hu, Y.; Yang, K.; Hu, M.; Zhou, D.; Guan, J., Synthesis, growth mechanism and optical properties of (K, Na) NbO 3 nanostructures. *CrystEngComm* **2010,** *12* (10), 3157-3162.

86. Skjærvø, S. L.; Wells, K. H.; Van Beek, W.; Grande, T.; Einarsrud, M.-A., Kinetics during hydrothermal synthesis of nanosized K x Na 1− x NbO 3. *CrystEngComm* **2018,** *20* (42), 6795-6802.

87. Banfield, J. F.; Welch, S. A.; Zhang, H.; Ebert, T. T.; Penn, R. L., Aggregation-based crystal growth and microstructure development in natural iron oxyhydroxide biomineralization products. *Science* **2000,** *289* (5480), 751-754.

88. Shi, G.; Wang, J.; Wang, H.; Wu, Z.; Wu, H., Hydrothermal synthesis of morphology-controlled KNbO3, NaNbO3, and (K, Na) NbO3 powders. *Ceramics International* **2017,** *43* (9), 7222-7230.

89. Alivisatos, A., Naturally aligned nanocrystals. *Science* **2000,** *289* (5480), 736-737.

90. Wang, C.; Hou, Y.; Ge, H.; Zhu, M.; Wang, H.; Yan, H., Sol–gel synthesis and characterization of lead-free LNKN nanocrystalline powder. *Journal of Crystal Growth* **2008,** *310* (22), 4635-4639.

91. Feizpour, M.; Bafrooei, H. B.; Hayati, R.; Ebadzadeh, T., Microwave-assisted synthesis and sintering of potassium sodium niobate lead-free piezoelectric ceramics. *Ceramics International* **2014,** *40* (1), 871-877.

92. Wang, H.; Liang, Z.; Liu, Q.; Zhang, D.; Wang, J., Synthesis, structure and photocatalytic hydrogen evolution of a silver-linked hexaniobate Lindqvist chain. *Inorganic Chemistry Communications* **2015,** *61*, 157-159.

93. Tong, H.; Ye, J., Building niobate nanoparticles with hexaniobate Lindqvist ions. Wiley Online Library: 2010.

94. De Andrade, J.; Pinheiro, A.; Vasconcelos, I.; De Araújo, M.; Valente, M.; Sombra, A., Structural studies of KNbO3 in niobate glass-ceramics. *Journal of Physics and Chemistry of Solids* **2000,** *61* (6), 899-906.

95. Chen, H.-J.; Chen, Y.-W., Hydrothermal synthesis of barium titanate. *Industrial & engineering chemistry research* **2003,** *42* (3), 473-483.

96.   Hakuta, Y.; Ura, H.; Hayashi, H.; Arai, K., Continuous production of BaTiO3 nanoparticles by hydrothermal synthesis. *Industrial & engineering chemistry research* **2005,** *44* (4), 840-846.

97.   Kumazawa, H.; Maeda, Y.; Sada, E., Further consideration of hydrothermal synthesis of barium ferrite fine particles. *Journal of materials science letters* **1995,** *14* (1), 68-70.

98.   Wang, Y.; Yu, E.; Yang, H.; Zhang, Q., Growth behavior of Li & Sb doped alkalis niobate synthesized by hydrothermal method. *Materials & Design* **2016,** *110*, 51-59.

99.   Sun, C.; Xing, X.; Chen, J.; Deng, J.; Li, L.; Yu, R.; Qiao, L.; Liu, G., Hydrothermal synthesis of single crystalline (K, Na) NbO3 powders. Wiley Online Library: 2007.

100.   Zhu, H.; Zheng, Z.; Gao, X.; Huang, Y.; Yan, Z.; Zou, J.; Yin, H.; Zou, Q.; Kable, S. H.; Zhao, J., Structural evolution in a hydrothermal reaction between Nb2O5 and NaOH solution: from Nb2O5 grains to microporous Na2Nb2O6.2/3H2O fibers and NaNbO3 cubes. *Journal of the American Chemical Society* **2006,** *128* (7), 2373-2384.

101.   Goh, G. K.; Lange, F. F.; Haile, S. M.; Levi, C. G., Hydrothermal synthesis of KNbO 3 and NaNbO 3 powders. *Journal of materials research* **2003,** *18* (2), 338-345.

102.   Wu, S.; Zhang, W.; Chen, X., Formation mechanism of NaNbO 3 powders during hydrothermal synthesis. *Journal of Materials Science: Materials in Electronics* **2010,** *21* (5), 450-455.

103.   Kong, X.; Hu, D.; Wen, P.; Ishii, T.; Tanaka, Y.; Feng, Q., Transformation of potassium Lindquist hexaniobate to various potassium niobates: solvothermal synthesis and structural evolution mechanism. *Dalton Transactions* **2013,** *42* (21), 7699-7709.

104.   Skjærvø, S. L.; Ong, G. K.; Grendal, O. G.; Wells, K. H.; van Beek, W.; Ohara, K.; Milliron, D. J.; Tominaka, S.; Grande, T.; Einarsrud, M.-A., Understanding the Hydrothermal Formation of NaNbO3: Its Full Reaction Scheme and Kinetics. *Inorganic Chemistry* **2021**.

105.   Gu, Q.; Lu, W.; Sun, Q.; Zhu, K.; Wang, J.; Liu, J.; Zhang, J.; Zeng, K.; Wang, J., Revealing the hydrothermal crystallization mechanism of ilmenite-type sodium niobate microplates: the roles of potassium ions. *CrystEngComm* **2017,** *19* (40), 5966-5972.

106.   Magrez, A.; Vasco, E.; Seo, J. W.; Dieker, C.; Setter, N.; Forro, L., Growth of single-crystalline KNbO3 nanostructures. *The Journal of Physical Chemistry B* **2006,** *110* (1), 58-61.

107.   Ahn, Z. S.; Schulze, W. A., Conventionally sintered (Na0. 5, K0. 5) NbO3 with barium additions. *Journal of the American Ceramic Society* **1987,** *70* (1), C-18-C-21.

108.   Liu, L.; Fan, H.; Fang, L.; Dammak, H.; Pham-Thi, M., Dielectric characteristic of nanocrystalline Na 0.5 K 0.5 NbO 3 ceramic green body. *Journal of electroceramics* **2012,** *28* (2-3), 144-148.

109.   Chowdhury, A.; Bould, J.; Londesborough, M. G.; Milne, S. J., Fundamental issues in the synthesis of ferroelectric Na0. 5K0. 5NbO3 thin films by sol− gel processing. *Chemistry of Materials* **2010,** *22* (13), 3862-3874.

110.   Chowdhury, A.; Bould, J.; Londesborough, M. G.; Milne, S. J., The effect of refluxing on the alkoxide-based sodium potassium niobate sol–gel system: Thermal and spectroscopic studies. *Journal of Solid State Chemistry* **2011,** *184* (2), 317-324.

111.   Chowdhury, A.; Bould, J.; Zhang, Y.; James, C.; Milne, S. J., Nano-powders of Na 0.5 K 0.5 NbO 3 made by a sol–gel method. *Journal of Nanoparticle Research* **2010,** *12* (1), 209-215.

112.   Khorrami, G. H.; Kompany, A.; Zak, A. K., Structural and optical properties of (K, Na) NbO3 nanoparticles synthesized by a modified sol–gel method using starch media. *Advanced powder technology* **2015,** *26* (1), 113-118.